Molecular Cell

Article

Metabolic enzyme UAP1 mediates IRF3 pyrophosphorylation to facilitate innate immune response

Graphical abstract

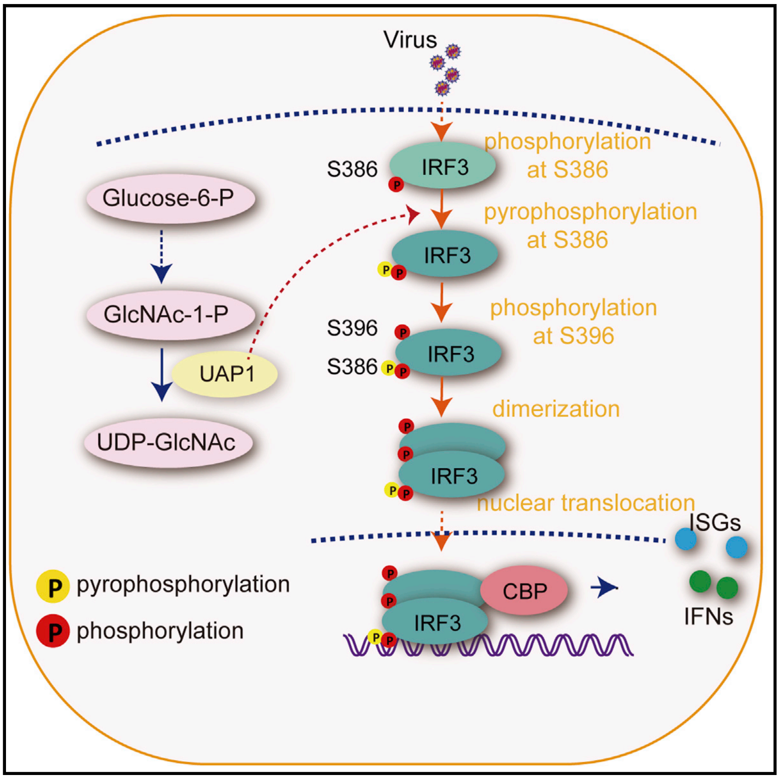

Authors

Shuai Yang, Shouheng Jin,
Huifang Xian, ..., Liang Zhou,
Mengqiu Li, Jun Cui

Correspondence

cuij5@mail.sysu.edu.cn

In brief

Yang et al. identify UAP1 as a pyrophosphorylase for protein serine pyrophosphorylation and demonstrate that UAP1-mediated IRF3 pyrophosphorylation is essential to promote robust type I interferon responses. They uncover the function of protein pyrophosphorylation in antiviral responses and provide insights into the crosstalk between metabolism and innate immunity.

Highlights

- UAP1 is a positive regulator of type I interferon signaling
- UAP1 catalyzes IRF3 pyrophosphorylation at serine 386
- UAP1 pyrophosphorylates IRF3 at S386 to promote antiviral responses

Yang et al., 2023, Molecular Cell *83*, 298–313
January 19, 2023 © 2022 Elsevier Inc.
https://doi.org/10.1016/j.molcel.2022.12.007

CellPress

CellPress

Molecular Cell

Article

Metabolic enzyme UAP1 mediates IRF3 pyrophosphorylation to facilitate innate immune response

Shuai Yang,[1] Shouheng Jin,[1] Huifang Xian,[1,2] Zhiyao Zhao,[1,2] Liqiu Wang,[1] Yaoxing Wu,[1] Liang Zhou,[1] Mengqiu Li,[1] and Jun Cui[1,3,*]

[1]Guangdong Province Key Laboratory of Pharmaceutical Functional Genes, MOE Key Laboratory of Gene Function and Regulation, State Key Laboratory of Biocontrol, School of Life Sciences, Sun Yat-sen University, Guangzhou, Guangdong, China

[2]Department of Gastroenterology, Guangzhou Institute of Pediatrics, Guangzhou Women and Children's Medical Center, Guangzhou Medical University, Guangzhou, Guangdong, China

[3]Lead contact

*Correspondence: cuij5@mail.sysu.edu.cn

https://doi.org/10.1016/j.molcel.2022.12.007

SUMMARY

Post-translational modifications (PTMs) of proteins are crucial to guarantee the proper biological functions in immune responses. Although protein phosphorylation has been extensively studied, our current knowledge of protein pyrophosphorylation, which occurs based on phosphorylation, is very limited. Protein pyrophosphorylation is originally considered to be a non-enzymatic process, and its function in immune signaling is unknown. Here, we identify a metabolic enzyme, UDP-N-acetylglucosamine pyrophosphorylase 1 (UAP1), as a pyrophosphorylase for protein serine pyrophosphorylation, by catalyzing the pyrophosphorylation of interferon regulatory factor 3 (IRF3) at serine (Ser) 386 to promote robust type I interferon (IFN) responses. *Uap1* deficiency significantly impairs the activation of both DNA- and RNA-viruse-induced type I IFN pathways, and the *Uap1*-deficient mice are highly susceptible to lethal viral infection. Our findings demonstrate the function of protein pyrophosphorylation in the regulation of antiviral responses and provide insights into the crosstalk between metabolism and innate immunity.

INTRODUCTION

Innate immune response induced by pathogen-associated molecular patterns (PAMPs) is the first line of host immune defenses.[1] Upon viral infection, pattern recognition receptors (PRRs) are employed to detect viral nucleic acids and then hierarchically trigger the signaling cascades, leading to the activation of downstream transcription factors, including interferon (IFN) regulatory factor 3 (IRF3) and nuclear factor κ-light-chain enhancer of activated B cells (NF-κB), to produce type I IFNs and proinflammatory cytokines. Secreted IFNs induce the transcription of hundreds of IFN-stimulated genes (ISGs), thus establishing the innate immune state against invading microbes.[2,3] The innate immune signaling must be activated in a timely manner to establish effective immunity to pathogens and then turned off to avoid excessive and potentially harmful immune responses.

Since immune cells experience dynamic and adaptive metabolic changes throughout their life cycles, metabolic programming in immune cells has become as an important determinant for immune recognition, signaling and responses through distinct signaling pathways.[4,5] Post-translational modification (PTM) of proteins by metabolites is the key output for metabolic change in innate immunity.[6] It has been reported that palmitoylation of STING (stimulator of interferon genes) at the Golgi is essential for activation of STING to provoke type I IFN production.[7] O-GlcNAcylation of MAVS (mitochondrial antiviral signaling protein) is required for K63-linked ubiquitination of MAVS and subsequent downstream antiviral signaling activation.[8] Although a set of PTMs has been uncovered to modulate innate immunity in different contexts, the function and underlying regulatory mechanisms of non-canonical metabolic modifications in innate immune responses remain poorly defined.

Protein pyrophosphorylation is a newly discovered PTM driven by inositol pyrophosphates.[9,10] It is currently believed that protein pyrophosphorylation is generated by a two-step reaction: the serine residue is first phosphorylated by kinase that provides a phosphoserine/phosphotyrosine residue and then diphosphoinositol pentakisphosphate (IP_7) transfers the β-phosphate group to the phosphoserine/phosphotyrosine through the Mg^{2+} cofactor.[11] Up to now, little is known about the role of protein pyrophosphorylation in cell signaling and the enzyme responsible for protein pyrophosphorylation has not been identified, thus protein pyrophosphorylation is considered to be a non-enzymatic process. It has been reported that

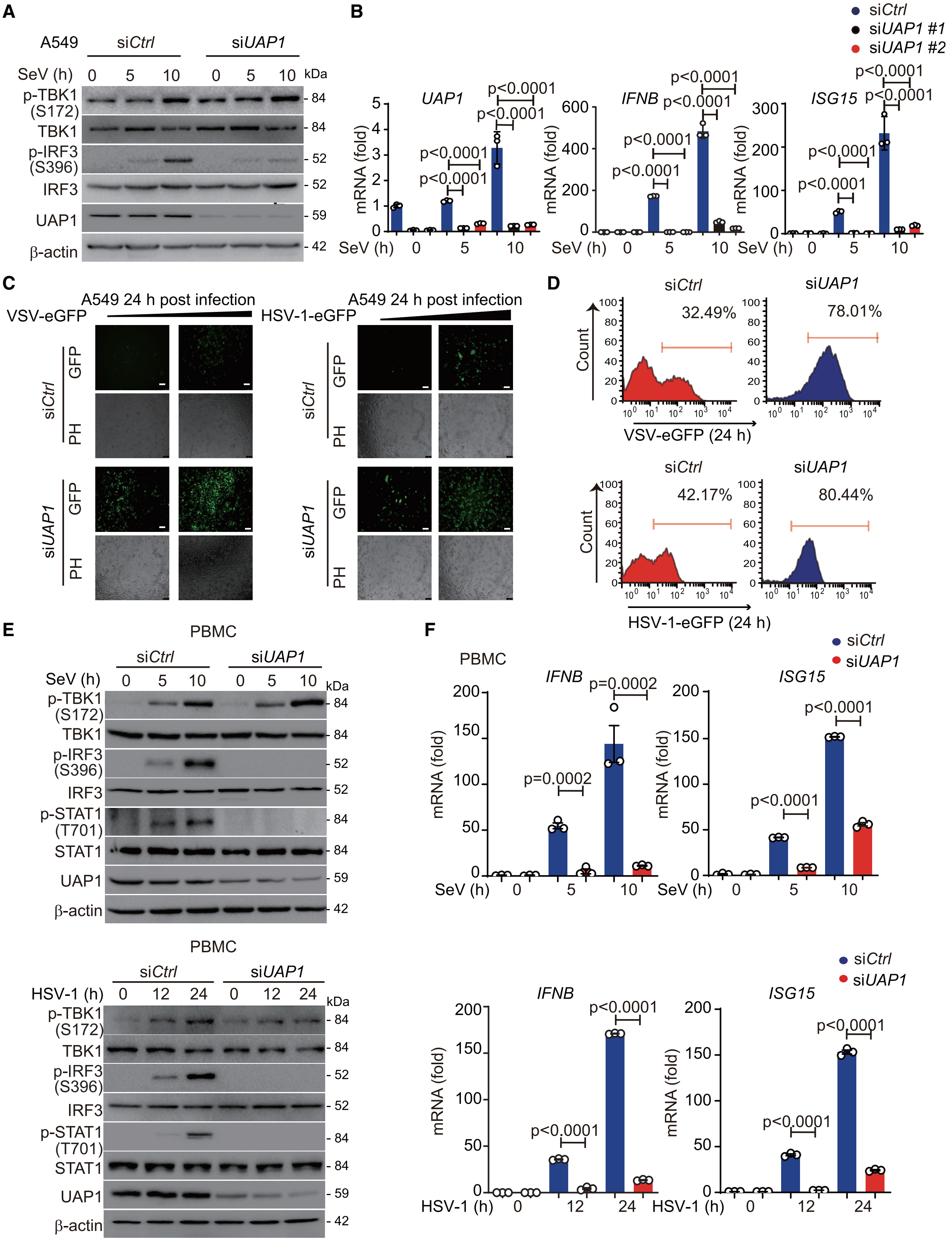

(legend on next page)

pyrophosphorylation of β subunit of adapter protein 3 prevents its interaction with kinesin-like protein 3A, thereby inhibiting HIV-1-virus-like particles release from the host cells.[12] Another report showed that pyrophosphorylation of dynein serves as a regulatory signal to enhance dynein-driven transport.[13] Whether immune factors can undergo protein pyrophosphorylation has not been explored yet.

Here, we identified UDP-N-acetylglucosamine pyrophosphorylase 1 (UAP1) as a positive regulator of innate immune responses against viruses. Overexpression of UAP1 facilitated the antiviral innate immune signaling and *Uap1* deficient mice produced less type I IFNs and were highly susceptible to lethal viral infection. Furthermore, we found that UAP1 directly catalyzed the pyrophosphorylation of IRF3 as a pyrophosphorylase. UAP1-mediated IRF3 pyrophosphorylation at Ser 386 was a required step for its subsequent phosphorylation of Ser 396 as well as the dimerization of IRF3. Taken together, our findings uncovered UAP1 as an important pyrophosphorylase for IRF3 pyrophosphorylation to promote the activation of type I IFN signaling and innate antiviral responses.

RESULTS

UAP1 is an essential positive regulator of type I IFN signaling

To delineate the comprehensive roles of metabolism-related enzymes and metabolic modification in innate immunity, we investigated the functions of a panel of glucose metabolism-related genes (GMRGs) through a single-guide RNAs (sgRNAs) screening system (Figure S1A). Among them, we identified UAP1 as a potent positive regulator that specifically modulates antiviral immunity (Figures S1B and S1C). UAP1 is the pyrophosphorylase in the last step of hexosamine biosynthetic pathway (HBP) and catalyzes the reaction of UTP and GlcNAc-1-P to synthesize diphosphate and UDP-GlcNAc, respectively.[14,15] Whether UAP1 functions in the regulation of immune responses is unknown.

We performed IFN-β and IFN-stimulated response element (ISRE) promoter-driven luciferase reporter assay and found that UAP1 potently enhanced type I IFN activation in a dose-dependent manner under infection of influenza virus (H1N1), Sendai virus (SeV), or vesicular stomatitis virus (VSV), or treatment with intracellular (IC) poly (I:C) or poly (dA:dT) (Figure S1D). Ectopic UAP1 enhanced IRF3 phosphorylation upon SeV infection (unless otherwise noted, phosphorylation of IRF3 was detected at position S396), while *UAP1* deficiency showed an opposite effect (Figures 1A and S1E). In addition, we found that knockdown of *UAP1* resulted in less expression of *IFNB* and *ISG15* mRNAs upon SeV infection compared with control group (Figure 1B). To further assess the antiviral ability of UAP1, we infected wild type (WT) and *UAP1*-knockdown A549 cells with VSV-eGFP or HSV-1-eGFP and observed a markedly enhanced viral load in *UAP1*-knockdown A549 cells through fluorescence microscopy and flow cytometry analysis (Figures 1C and 1D).

To determine the role of UAP1 under physiological conditions, we efficiently knocked down *UAP1* in human peripheral blood mononuclear cells (PBMCs) and found that *UAP1* deficiency markedly inhibited IRF3 phosphorylation under SeV or HSV-1 infection (Figure 1E). Furthermore, the expression of *IFNB* and *ISG15* mRNAs were markedly reduced upon SeV or HSV-1 infection in *UAP1* knockdown PBMCs (Figure 1F). Additionally, knockdown of *UAP1* in PBMCs significantly decreased IFN-β secretion induced by SeV, HSV-1, H1N1, Dengue virus (DENV), or Zika virus (ZIKV) (Figure S1F). Taken together, these results suggest that UAP1 is a universal positive regulator of type I IFN signaling against viral infection.

Uap1 deficiency inhibits antiviral immunity *in vivo*

To further unveil the function of UAP1 in virus-triggered innate immune signaling, we generated *Uap1*-deficient mice using a CRISPR-Cas9-based system (Figure S2A). According to the IMPC (International Mouse Phenotyping Consortium) datasets (https://www.mousephenotype.org/), *Uap1*$^{-/-}$ embryos die at organogenesis (E9.5). We counted 88 mice and found 29 WT (*Uap1*$^{+/+}$), 59 heterozygote (*Uap1*$^{+/-}$) and 0 homozygote (*Uap1*$^{-/-}$) offspring. Genotype ratio of the offspring matched the Mendel's law of inheritance, implicating that *Uap1* deletion is incompatible with normal mouse embryonic development (Figure S2B). Interestingly, we found the protein level of UAP1 is markedly reduced in *Uap1*$^{+/-}$ bone-marrow-derived macrophages (BMDMs), bone-marrow-derived dendritic cells (BMDCs) and peritoneal macrophages (PEMs) (Figure S2C), suggesting *Uap1*$^{+/-}$ mice is a good knockdown model to study the function of UAP1 *in vivo*.

We next infected BMDMs with SeV or HSV-1 and found that *Uap1* deficiency markedly inhibited the phosphorylation levels of IRF3 other than TBK1 (TANK-binding kinase 1) (Figure 2A). Global RNA sequencing (RNA-seq) analysis was used to identify genes and pathways regulated by UAP1. Gene ontology enrichment analysis showed significant enrichment

Figure 1. UAP1 positively regulates virus-induced type I IFN signaling

(A) Immunoblot analysis of A549 cells transfected with control siRNA (si*Ctrl*) or *UAP1*-specific siRNA (si*UAP1*), followed by infection with SeV (multiplicity of infection [MOI] = 1) for indicated time periods with the indicated antibodies.

(B) Quantitative reverse transcription and polymerase chain reaction (qRT-PCR) analysis of *IFNB*, *ISG15*, and *UAP1* mRNAs in A549 cells treated with si*Ctrl* or si*UAP1*, followed by infection with SeV (MOI = 1) for indicated time periods.

(C and D) Phase-contrast (PH) and fluorescence microscopy (C) and flow cytometric analysis (D) of A549 cells transfected with si*Ctrl* or si*UAP1*, and then infected with VSV-eGFP (MOI = 1) or HSV-1-eGFP (MOI = 1). Scale bars, 50 μm.

(E) Immunoblot analysis of peripheral blood mononuclear cells (PBMCs) transfected with si*Ctrl* or si*UAP1*, followed by SeV (MOI = 1) or HSV-1 (MOI = 1) infection, at indicated time periods.

(F) qRT-PCR analysis of *IFNB* and *ISG15* mRNA levels in PBMCs transfected with si*Ctrl* or si*UAP1*, followed by infection with SeV (MOI = 1) or HSV-1 (MOI = 1) at indicated time periods.

Data in (B) and (F) are expressed as mean ± SEM of three independent experiments. p values were determined by unpaired two-tailed Student's t test. All other experiments are representatives of three independent biological experiments with similar results.

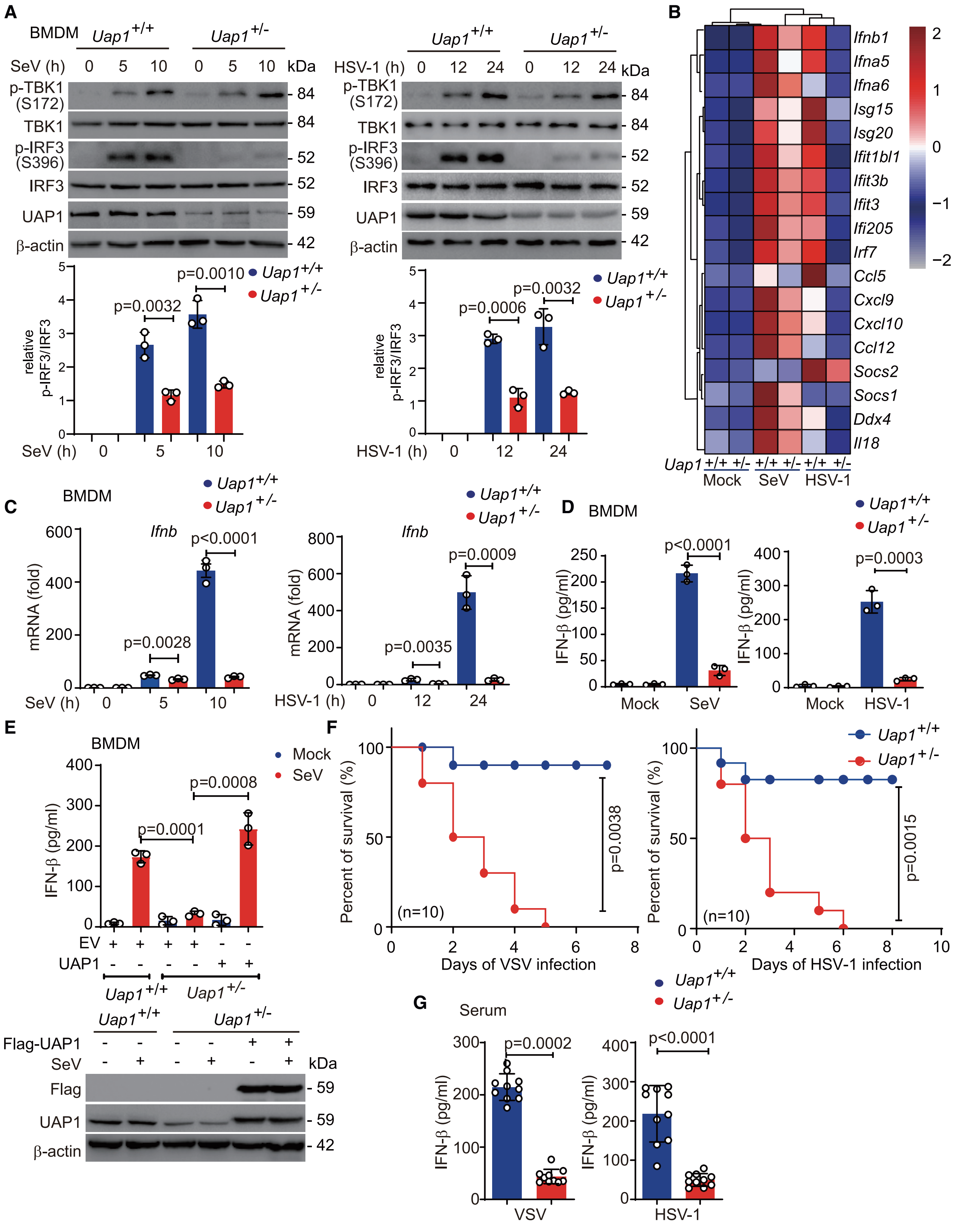

(legend on next page)

for immune-response functions and metabolism (Figures S2D and S2E). The heatmap of antiviral-related genes also revealed that *Uap1* deficiency inhibited a variety of ISGs upon viral infection (Figures 2B and S2F), which are also defined in the interferome database.[16] Consistently, *Ifnb* transcription and IFN-β secretion induced by SeV or HSV-1 infection were significantly decreased in *Uap1*$^{+/-}$ BMDMs (Figures 2C and 2D). Reintroducing UAP1 in *Uap1*-deficient BMDMs restored its ability to secrete IFN-β (Figure 2E). These data indicate a positive role of UAP1 in antiviral immunity against both RNA and DNA viruses in primary cells.

To investigate the functional significance of UAP1 in host antiviral response *in vivo*, we challenged *Uap1*$^{+/-}$ mice with VSV or HSV-1, and histological analysis showed greater infiltration of immune cells and injury of lung and liver in *Uap1*$^{+/-}$ mice (Figure S3A). We also observed a greater decrease of phosphorylated IRF3 level (Figures S3B and S3C) and more viral replication (Figures S3D and S3E) in liver and lung in *Uap1*$^{+/-}$ mice after VSV infection. *Uap1*$^{+/-}$ mice were highly susceptible to VSV or HSV-1 infection in overall survival assays than that in *Uap1*$^{+/+}$ mice (Figure 2F). Consistent with the decreased resistance, *Uap1*$^{+/-}$ mice produced lower levels of IFN-β than WT mice in response to VSV or HSV-1 infection (Figure 2G). Taken together, these results demonstrate that *UAP1* deficiency impaired innate antiviral responses against viral infection by producing less IFN-β *in vivo*.

UAP1 interacts with IRF3

To determine the molecular mechanism by which UAP1 promotes type I IFN signaling, we performed luciferase reporter assay and found that UAP1 promoted the luciferase reporter activity induced by RIG-I-N (N-terminal caspase recruitment domain of retinoic acidinducible gene-1 [RIG-I], an active deletion of RIG-I), MAVS, TBK1, but not IRF3 (5D) (a constitutively active mutant of IRF3) (Figure 3A). Immunoprecipitation (IP) and immunoblot analysis revealed that UAP1 strongly interacted with IRF3, but not other molecules in type I IFN signaling (Figure 3B). To rigorously observe the physiological relevance of these findings, we infected A549 cells and BMDMs with SeV or HSV-1 and observed the enhanced interaction between endogenous UAP1 and IRF3 after virus infection (Figures 3C–3F). To determine whether the interaction between UAP1 and IRF3 is direct, we performed an *in vitro* binding assay and found recombinant His-IRF3 directly interacted with purified Flag-tagged UAP1 (Figure 3G). In addition, we found that UAP1 was prone to interact with phosphorylated IRF3 (p-IRF3) (Figure 3H). We next tested the interaction between UAP1 and IRF3 in *TBK1*-knockout (KO) HEK293T cells and observed that the interaction between UAP1 and IRF3 did not change upon viral infection (Figure 3I). To further determine UAP1-IRF3 interaction, we used a fluorescence resonance energy transfer (FRET) assay to analyze FRET efficiency values (E-FRET) between YFP-IRF3 and CFP-UAP1 upon viral infection.[17] We observed that the average E-FRET (3 h upon viral infection) was increased obviously in the cytoplasm in virus-infected cells in comparison with that in untreated cells (Figure 3J). To identify which domain of IRF3 is responsible for its interaction with UAP1, we generated several deletion constructs of IRF3. IP and immunoblot analysis revealed that the IR domain (including IRF association domain and regulatory domain) of IRF3 interacted with UAP1, but its DP domain (including DNA-binding domain and proline-rich domain) showed no interaction with UAP1 (Figure 3K). Collectively, these results suggest that UAP1 directly targets IRF3 upon viral infection.

The enzyme activity of UAP1 is required to potentiate antiviral signaling

We next investigated whether UAP1 regulates type I IFN signaling pathway via its pyrophosphorylase activity. We generated pyrophosphatase-inactive mutants of UAP1 by substituting the corresponding lysine (K) or arginine (R) with alanine (A) as previously described,[18] and confirmed that they no longer promoted global protein O-GlcNAcylation (Figures S4A and S4B). Interestingly, we found that although the inactive mutants of UAP1 could still interact with IRF3, they failed to prompt IRF3 phosphorylation anymore (Figures 4A and S4C). Consistently, mutations of UAP1 enzymatic sites abrogated its ability to upregulate type I IFN signaling under viral infection (Figures 4B and 4C). We next found that UAP1 was indispensable for cell growth by lactate dehydrogenase release (LDH) assay (Figure S4D). This result is consistent with a previous report that lack of UDP-GlcNAc leads to cell death.[19,20] To generate *UAP1* KO cells, we added UDP-GlcNAc to sg*UAP1* HEK293T cells for drug selection and found that reintroducing UDP-GlcNAc rescued the viability of sg*UAP1* cells (Figure S4D). Based on this method, we generated viable *UAP1* KO cells (Figure S4E) for following experiments. Consistently, mutations of UAP1 enzymatic sites

Figure 2. *Uap1* deficiency inhibits antiviral immunity *in vivo*

(A) Immunoblot analysis of indicated proteins in bone-marrow-derived macrophages (BMDMs) from *Uap1*$^{+/+}$ or *Uap1*$^{+/-}$ mice following infection with SeV (MOI = 1) or HSV-1 (MOI = 1) for indicated time periods.

(B) Heatmaps showing the expression (RNA-seq; maximum to minimum, normalized) of type I IFNs and IFN-stimulated genes in *Uap1*$^{+/+}$ or *Uap1*$^{+/-}$ BMDMs infected with SeV (MOI = 1) for 5 h or HSV-1 (MOI = 1) for 12 h.

(C) Quantitative reverse transcription and polymerase chain reaction (qRT-PCR) analysis of *Ifnb* in BMDMs from *Uap1*$^{+/+}$ or *Uap1*$^{+/-}$ mice stimulated with SeV (MOI = 1) or HSV-1 (MOI = 1) for indicated time periods.

(D) ELISA of IFN-β secretion in BMDMs from *Uap1*$^{+/+}$ or *Uap1*$^{+/-}$ mice stimulated with SeV (MOI = 1) for 10 h or HSV-1 (MOI = 1) for 24 h.

(E) ELISA of IFN-β secretion (top) and immunoblot analysis (bottom) in *Uap1*$^{+/+}$ or *Uap1*$^{+/-}$ BMDMs transfected with plasmid encoding UAP1 or empty vector, followed by infection with SeV (MOI = 1) for 10 h.

(F) Survival curve of 8-week-old *Uap1*$^{+/+}$ or *Uap1*$^{+/-}$ mice given intravenously injection of VSV (1×10^8 pfu/g) or HSV-1 (2×10^7 pfu/g) (n = 10 per group).

(G) IFN-β levels were analyzed by ELISA in the serum of *Uap1*$^{+/+}$ or *Uap1*$^{+/-}$ mice (n = 10 per group), which were intravenously injected with VSV (1×10^8 pfu/g) or HSV-1 (2×10^7 pfu/g) for 24 h.

Data in (A) and (C)–(E) are expressed as means ± SEM of at least three independent experiments. Data in (G) are expressed as mean values ± SD (n = 10 mice per group). p values were determined by unpaired two-tailed Student's t test. Other experiments are representatives of three independent biological experiments with similar results.

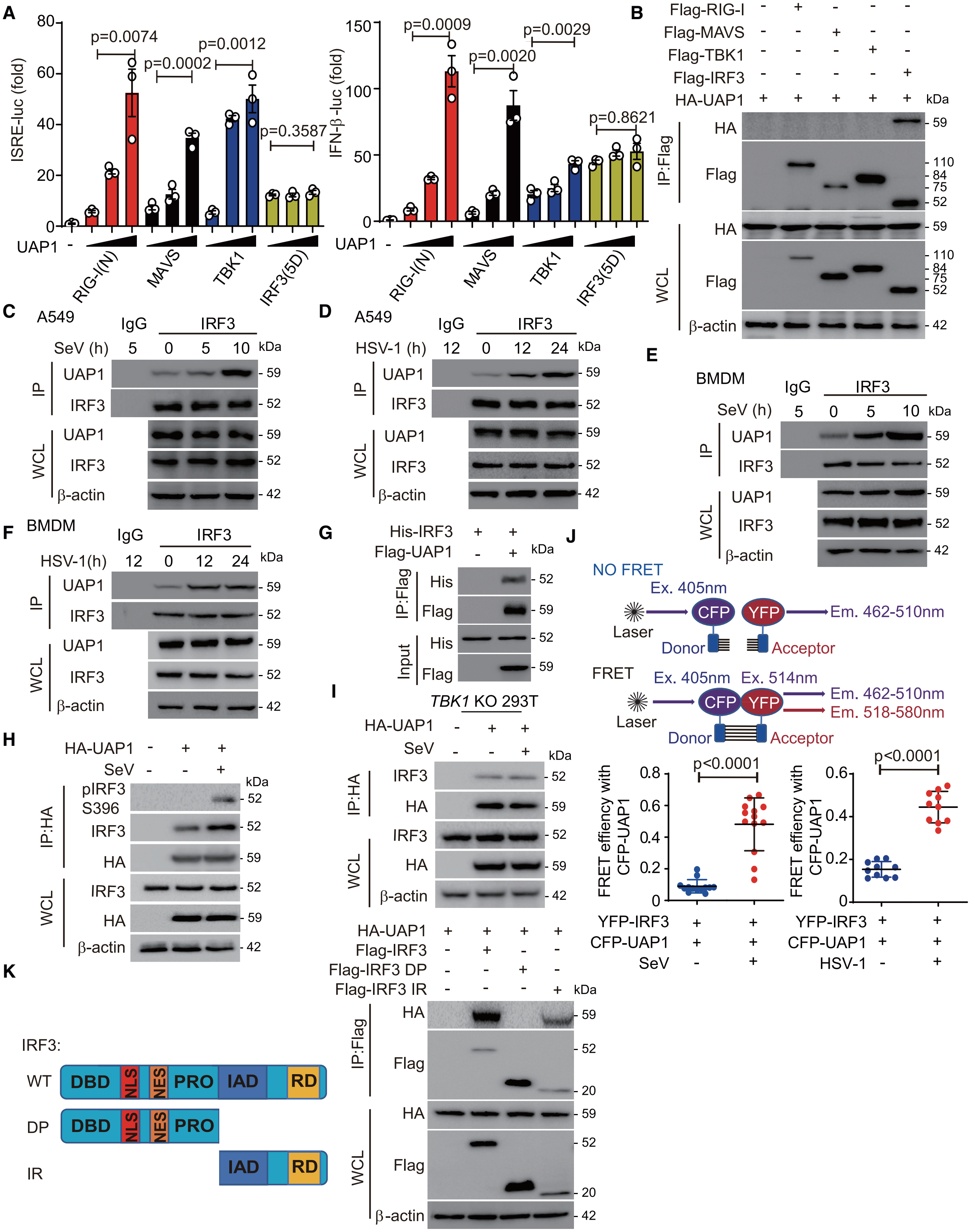

(legend on next page)

abrogated its ability to upregulate type I IFN signaling under viral infection (Figure 4D). These findings demonstrate that UAP1 serves as a positive regulator in type I IFN signaling via its pyrophosphatase activity.

Since UAP1 could provide UDP-GlcNAc for both O-GlcNAcylation and N-GlcNAcylation, and recent reports showed that O-GlcNAc transferase (OGT) regulates the O-GlcNAcylation of MAVS to enhance type I IFN signaling,[8,21] we then investigated whether UAP1 mediates type I IFN activation by promoting O-GlcNAcylation or N-GlcNAcylation of IRF3. As expected, we found that knockdown of *UAP1* inhibited the abundance of UDP-GlcNAc (Figure S4F). HEK293T cells were pretreated with UDP-GlcNAc (within the concentration of 100 μM) to replenish the protein glycosylation according to previous works,[22,23] and the amount of UDP-GlcNAc we added was sufficient to maintain the similar IC UDP-GlcNAc abundance in both control and *UAP1*-deficient cells (Figure S4G). Although UDP-GlcNAc treatment globally enhanced the phosphorylation of IRF3 and STAT1 upon viral infection, which is consistent with previous report,[23] we found that *UAP1* deficiency could still inhibit the phosphorylation of IRF3 and STAT1 in UDP-GlcNAc-pretreated cells (Figure S4H). In consistent with these results, we found that *UAP1* deficiency could still inhibit *IFN-β* and *ISG15* expression in UDP-GlcNAc-pretreated cells (Figure S4I). Meanwhile, *UAP1* deficiency had no effect on IRF3 O-GlcNAcylation, and the level of O-GlcNAcylation of IRF3 did not markedly change upon viral infection (Figures S4J and S4K). In addition, we treated the cells with OSMI-1 (an OGT inhibitor) or tunicamycin (TM, a N-GlcNAcylation inhibitor) and observed that UAP1 could still promote the activation of type I IFN signaling (Figures S4L and S4M). We further confirmed that KO of *UAP1* could still promote VSV and HSV-1 replication in UDP-GlcNAc-pretreated cells (Figure S4N). Taken together, these data suggest that UAP1 promotes type I IFN signaling in a GlcNAcylation-independent manner.

UAP1 catalyzes pyrophosphorylation of IRF3

As UAP1 is a pyrophosphorylase, we next investigated whether UAP1 directly influences the pyrophosphorylation of IRF3. The β-phosphate can be transferred from IP_7 to prephosphorylated proteins, to generate pyrophosphorylation.[24] Through molecular docking studies, we showed that UAP1 could bind to IP_7 (Figure S4O). We next used IP_6 kinase 1 (IP6K1) and [^{32}P] ATP to synthesize 5β[^{32}P] IP_7 and performed protein pyrophosphorylation assay as previously described.[10] We found p-IRF3 other than IRF3 can be further pyrophosphorylated by IP_7 only in the presence of UAP1, indicating that UAP1 is capable to mediate IRF3 pyrophosphorylation (Figure 4E). Moreover, we found that the inactive mutants of UAP1 failed to catalyze IRF3 pyrophosphorylation (Figure 4F). To further confirm this finding, we examined the total pyrosphosphate (intracellular pyrophosphate [PPi]) of purified IRF3 from *IRF3*-KO HEK293T cells by fluorimetric pyrophosphate assay, and observed apparent increase of IRF3-associated PPi in the presence of WT UAP1, but not its inactive mutants, upon SeV infection (Figure 4G). N2-(*m*-Trifluorobenzyl) (TNP) is a widely used inhibitor of IP6K1, which potently decreases pyrophosphorylation.[25] We pretreated cells with TNP and found that TNP inhibited the IRF3-associated PPi level (Figure 4H). To further investigate whether UAP1 acts as a protein pyrophosphorylase, we predicted multiple sites on UAP1 that might abrogate its binding ability with IRF3 through bioinformatic analysis by autodock vine and generated a serial of UAP1 mutants by replacing Glu303, Asn223 (which establish hydrogen bonds with sugar N-acetylarm), Asp253 (which is the side chain of the sequence conserved), Phe381 (which establishes hydrophobic interactions with sugar N-acetylarm), or Arg453 (which provides additional nucleotide-sugar-binding residues) with arginines. We found that UAP1 R453A mutant, which showed reduced binding ability with IRF3 (Figure S4P), did not affect O-GlcNAcylation (Figure S4Q). In consistent with this result, UAP1 R453A mutant, which did not affect UDP-GlcNAc synthesis, failed to promote type I IFN activation and IRF3 pyrophosphorylation at S386 (Figures S4R–S4T). These findings further confirmed that UAP1 functions as a pyrophosphorylase to regulate the antiviral response by mediating IRF3 pyrophosphorylation.

In line with the importance of UAP1 enzymatic activity in type I IFN signaling, pretreatment with TNP resulted in the inhibition of UAP1-mediated type I IFN activation (Figures 5A–5C).

Figure 3. UAP1 associates with IRF3

(A) Luciferase activity of HEK293T cells transfected with plasmids encoding IFN-stimulated response element (ISRE)-luc or IFN-β-luc reporter, together with RIG-I(N), MAVS, TBK1, or IRF3 (5D), along with empty vector (EV) or with increasing amounts of UAP1 vector.

(B) Immunoblot analysis of extracts of HEK293T cells transfected with plasmids encoding HA-tagged UAP1 and Flag-tagged EV, RIG-I, MAVS, TBK1, or IRF3, followed by immunoprecipitation (IP) with anti-Flag beads.

(C–F) Immunoblot analysis of A549 (C and D) or BMDMs (E and F) infected with SeV (MOI = 1) or HSV-1 (MOI = 1) for indicated time periods, followed by IP with anti-IRF3 antibody.

(G) *In vitro* binding assay of Flag-tagged UAP1 purified from HEK293T cells and His-tagged IRF3 purified from *E. coli*.

(H) Immunoblot analysis of extracts of HEK293T cells transfected with plasmids encoding HA-UAP1, after SeV (MOI = 1) infection for 5 h, followed by immunoprecipitation with anti-HA beads.

(I) Immunoblot analysis of extracts of *TBK1* knockout (KO) HEK293T cells transfected with plasmids encoding HA-UAP1, after SeV (MOI = 1) infection for 5 h, followed by immunoprecipitation with anti-HA beads.

(J) A549 cells were transfected with plasmids expressing CFP-UAP1 as fluorescence resonance energy transfer (FRET) donor and YFP-IRF3 as FRET acceptor. The FRET efficiency was calculated in A549 cells infected with SeV (MOI = 1) or HSV-1 (MOI = 1) for 3 h.

(K) Domain organization of IRF3 protein (left). Immunoblot analysis of extracts of HEK293T cells transfected with plasmids encoding HA-UAP1 together with Flag-IRF3, Flag-IRF3 DP, or Flag-IRF3 IR (right), followed by IP with anti-Flag beads.

Data in (A) are expressed as mean ± SEM of three independent experiments. Data in (J) are expressed as mean ± SD of 10 cells for each condition. p values were determined by unpaired two-tailed Student's t test. All other experiments are representatives of three independent biological experiments with similar results.

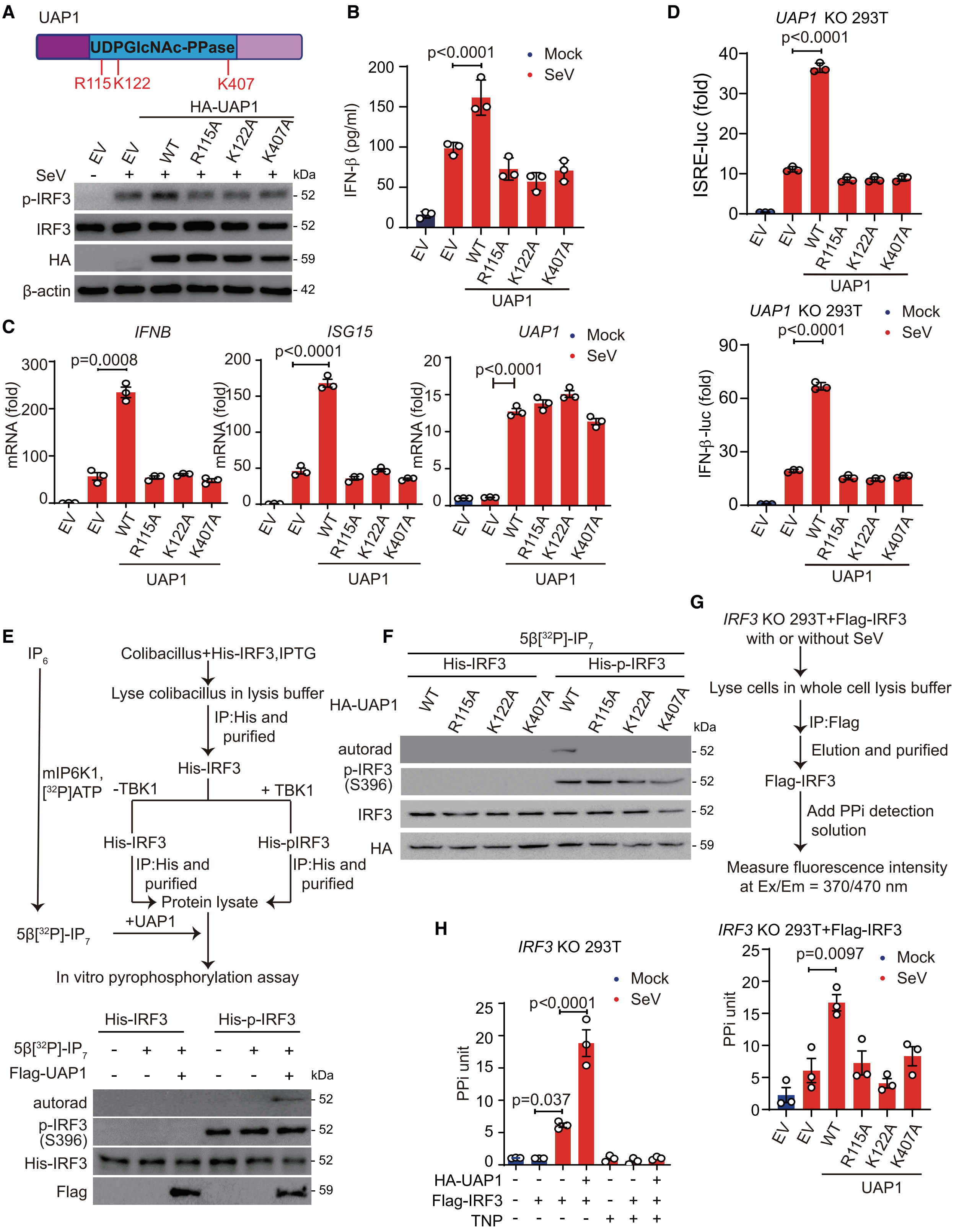

(legend on next page)

Consistently, TNP pretreatment suppressed the phosphorylation of IRF3 and STAT1 in BMDMs and A549 cells (Figures S5A and S5B). We next knocked down the expression of *IP6K1* and found that *IP6K1* deficiency also resulted in the inhibition of UAP1-mediated type I IFN activation (Figure S5C). In consistent with these results, KO of *IP6K1* promoted VSV replication, which is similar to that we observed in TNP treatment experiments (Figures S5D and S5E). These data suggest that TNP mainly affects cell signaling to inhibit antiviral responses.

We next examined the effects of TNP in host antiviral immune responses *in vivo*. Following an injection of TNP (20 mg/kg body weight [BW]) in mice, we challenged mice with VSV. Histological analysis showed greater infiltration of immune cells and injury of lung and liver in TNP group, compared with those in control group (Figure 5D). Consistently, viral load was significantly increased in the lung and liver of TNP-pretreated mice (Figures 5E and 5F). Additionally, we showed a greater decrease of *Ifnb* and *Isg15* levels in the lung and liver of TNP-pretreated mice (Figures 5G and 5H). We further found that TNP-pretreated mice were highly susceptible to VSV infection in overall survival assays compared with DMSO-pretreated mice (Figure 5I). We also observed the downregulation of IFN-β level in the serum of TNP-pretreated mice (Figure 5J). Taken together, these results indicate that UAP1-directed pyrophosphorylation of IRF3 potentiates antiviral responses.

Pyrophosphorylation facilitates IRF3 activation

It is well documented that the phosphorylation and dimerization of IRF3 are the necessary steps for its full activation. Given that IRF3 forms dimers after phosphorylation, we separated IRF3 monomers (less than 90 kDa) from dimers (greater than 90 kDa) by gel filtration of SeV-infected cell lysates and observed that *in-vitro*-purified UAP1 only interacted with IRF3 monomers but not IRF3 dimers (Figure 6A). Next, we found that *UAP1* deficiency impaired SeV-induced dimerization of IRF3 (Figure 6B). In addition, the nuclear translocation of IRF3 was markedly decreased in *Uap1*$^{+/-}$ BMDMs, compared with that in *Uap1*$^{+/+}$ BMDMs (Figures 6C and 6D). To evaluate whether this effect is caused by reduced pyrophosphorylation of IRF3, we pretreated cells with TNP and found that TNP also impaired the dimerization of IRF3 (Figure 6E). Consistently, TNP inhibited IRF3 transport into the nucleus (Figures 6F and 6G). These results were further confirmed by coIP that UAP1 enhanced SeV-induced IRF3 oligomerization (Figure 6H).

UAP1 pyrophosphorylates IRF3 at S386 to promote type I IFN signaling

We next sought to determine the detail molecular mechanisms by which UAP1 activates IRF3 through pyrophosphorylation. We examined the total PPi of purified IRF3 and its deletion constructs and found that the IR domain of IRF3 is critically required for its pyrophosphorylation (Figure S6A). Further study showed that IRF3-5D mutant, which led to constitutive activation of IRF3, and IRF3-5A mutant, which led to constitutive inactivation of IRF3, showed no influence on the pyrophosphorylation of IRF3 (Figures S6B and S6C). In addition, we showed that UAP1 could not affect the activity of IRF3-5D (Figure S6D). These results indicated that other sites remained to be identified for IRF3 pyrophosphorylation before these five sites are phosphorylated. We next applied mass spectrometry analysis to find that S386 and T390 on IRF3 could be pyrophosphorylated (Figure 7A), which is further confirmed by mutation experiments (Figure S6E). Interestingly, we found that T390A mutation of IRF3 showed no influence on the activation of IRF3, while S386A mutation of IRF3 not only abrogated the pyrophosphorylation of IRF3, but also markedly abrogated the type I IFN signaling (Figures 7B and S6F). We next generated a series of IRF3 phosphopeptides and checked whether UAP1 could catalyze the pyrophosphorylation of them. We found that UAP1 specifically mediated the pyrophosphorylation of pS386 peptide, but not other indicated peptides (Figure S6G). In addition, we tested the PPi of synthesized IRF3 pS386 peptide and found that the kit could successfully detect protein-linked pyrophosphate (Figure S6H), further supporting the finding of pyrophosphorylation of IRF3 at S386 both *in vitro* and in cells.

According to previous studies,[26,27] there are two classes of regulatory phosphorylation sites with different effects on transactivation activity located in the C-terminal region of IRF3: 2S

Figure 4. UAP1 mediates the pyrophosphorylation of IRF3

(A) Domain organization of UAP1 (top). Immunoblot analysis of extracts of HEK293T cells transfected with empty vector (EV) or plasmids encoding wild-type (WT) HA-UAP1 or its inactive mutants (R115A, K122A, or K407A) after SeV (MOI = 1) infection for 5 h (bottom).

(B) ELISA analysis of IFN-β secretion in HEK293T cells transfected with vectors of HA-UAP1 (WT, R115A, K122A, or K407A), followed by SeV (MOI = 1) infection for 10 h.

(C) qRT-PCR analysis of *IFNB*, *ISG15*, and *UAP1* mRNA level in HEK293T cells transfected with plasmids expressing HA-UAP1 (WT, R115A, K122A, or K407A), after SeV (MOI = 1) infection for 10 h.

(D) Luciferase activity of *UAP1* knockout (KO) HEK293T cells transfected with plasmids encoding ISRE-luc (top) or IFN-β-luc (bottom), together with WT UAP1 or its indicated mutants, after SeV (MOI = 1) infection for 10 h.

(E) Experimental setup for IRF3 pyrophosphorylation assay through autoradiography (top). Autoradiography was used to determine the protein pyrophosphorylation and immunoblot analysis was used to confirm the equal loading of indicated proteins (bottom).

(F) Pyrophosphorylation of IRF3 with indicated WT UAP1 and its mutants were measured by autoradiography *in vitro*.

(G) Experimental setup for the measurement of pyrophosphorylation of IRF3 by fluorimetry assay (top). Intracellular pyrophosphate (PPi) of IRF3 was measured in *IRF3* KO HEK293T cells transfected with vector of WT UAP1 or its indicated mutants together with Flag-IRF3 after infection with SeV (MOI = 1) for 5 h (bottom), followed by immunoprecipitation with anti-Flag beads.

(H) PPI of IRF3 was measured in *IRF3* KO HEK293T cells transfected with plasmid of HA-UAP1 or EV together with Flag-IRF3, pretreated with N^2-(*m*-Trifluorobenzyl) (TNP) (10 μM) together with SeV (MOI = 1) for 10 h, followed by immunoprecipitation with anti-Flag beads.

Data in (B)–(D), (G), and (H) are expressed as mean ± SEM of three independent experiments. p values were determined by unpaired two-tailed Student's t test. All other experiments are representatives of three independent biological experiments with similar results.

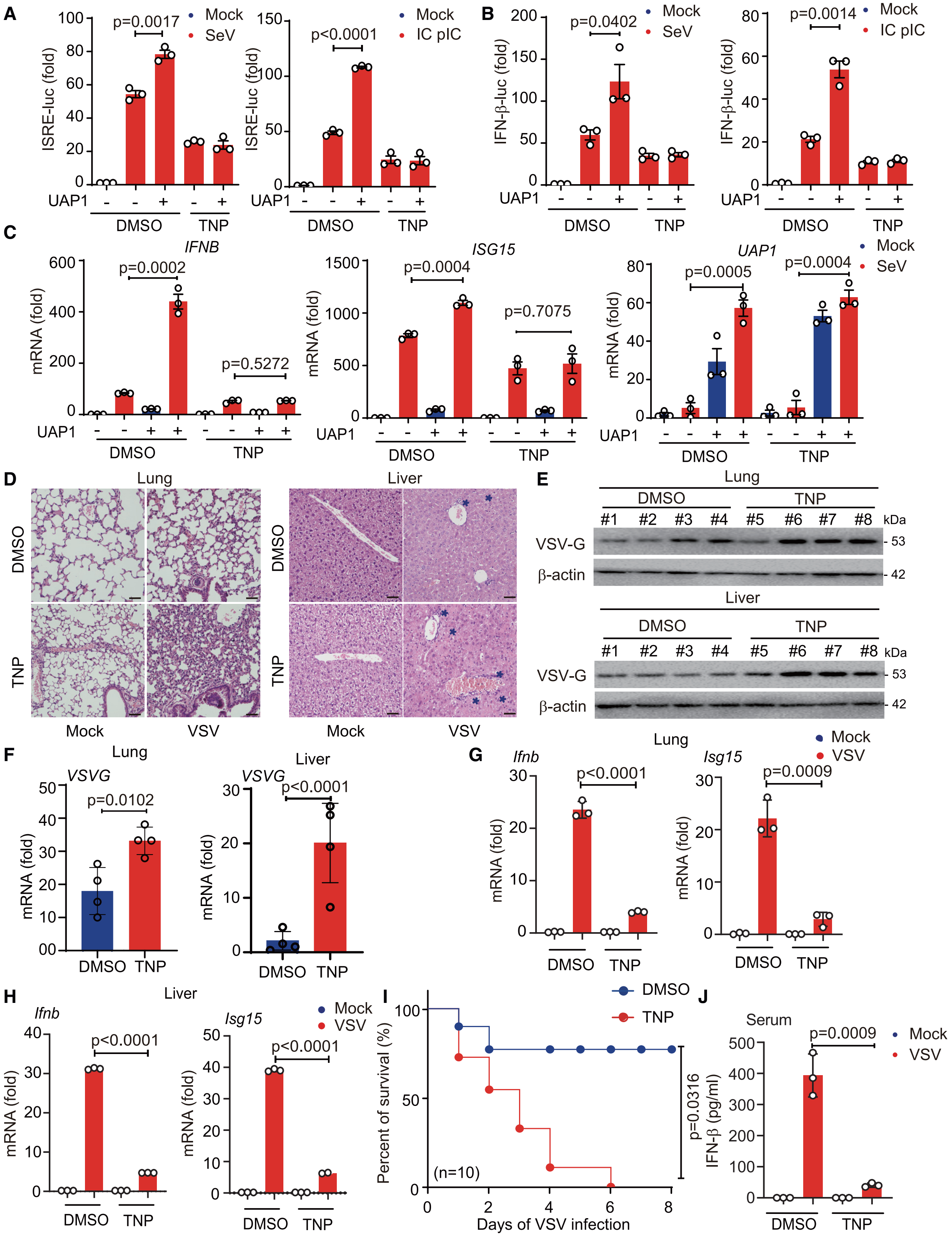

(legend on next page)

sites (S385 and S386) and 5ST sites (S396, S398, S402, T404, and S405) (Figure S6I). We wondered whether pyrophosphorylation of IRF3 at S386 serves as a signal for subsequent multi-site phosphorylation. We found that knockdown of *UAP1* or TNP treatment mainly reduced the phosphorylation of S396, but not S386 of IRF3, indicating the sequential event of IRF3 multi-site phosphorylation (Figures 7C and 7D). Further study showed that S386A mutation of IRF3 prevented the phosphorylation of S396 site, while S396A mutation showed no influence on the phosphorylation of S386 (Figure S6J). Taken together, these data demonstrate that UAP1-directed IRF3 pyrophosphorylation at S386 serves as a required step for subsequent S396 phosphorylation as well as dimerization of IRF3. According to previous studies,[26,28] the phospho-mimetic mutants with the substitution of S/T residues with aspartic acid (D) discharge the C-terminal inhibitory domain of IRF3 and prompt the dimerization and activation of IRF3. We next found that S386A/D mutation could not be pyrophosphorylated as efficiently as the WT IRF3 did (Figure 7E). To further demonstrate that phosphorylation of S386 is not enough for IRF3 activation, we mutated S386 to E386 according to a previous work[29] and found that S386E also failed to active IRF3 (Figure 7E). Consistently, UAP1 no longer enhanced type I IFN activation when IRF3 S386 is mutated (Figures 7F, S6K, and S6L). These results indicated that the phosphorylation of IRF3 at S386 is not enough to activate type I IFN signaling, which highlights the importance of pyrophosphorylation of IRF3 in antiviral immunity. We next checked the interaction between IRF3 and TBK1 with or without TNP treatment and found that TNP reduced the interaction between IRF3 and TBK1 (Figure S6M), indicating that the pyrophosphorylation of IRF3 on S386 enhanced the binding to TBK1, which might facilitate the phosphorylation of IRF3 S396 for its fully activation.

Taken together, our findings illuminate the regulatory mechanism of UAP1 in antiviral immunity. Upon viral infection, IRF3 undergoes pyrophosphorylation at S386 mediated by UAP1, which is required for subsequent phosphorylation at S396. Pyrophosphorylation of IRF3 worked as a checkpoint to control the dimerization of IRF3, thus turning on the robust type IFN signaling (Figure 7G).

DISCUSSION

The phosphorylation of IRF3 plays critical roles in determining the immune state and the cell fate against viral infection. Until now, the sequential activation mode of IRF3 through multi-site phosphorylation remains controversial. It has been reported that S385 and S386 of IRF3 are exposed to be first phosphorylated, leading to its conformational change,[28] while other studies indicated virus-induced phosphorylation of IRF3-5ST is an earlier event.[26] Here, we found IRF3 S396A mutant can be phosphorylated at S386, but IRF3 S386A mutant failed to be phosphorylated at S396, suggesting that the phosphorylation of IRF3-2S plays an earlier role in the regulation of IRF3-5ST phosphorylation and further supported the hypothesis of IRF3 sequential phosphorylation mode as previously described.[30] Interestingly, although IRF3 5D mimics its phosphorylated form with constitutive DNA binding and transactivation activities, the S385/386D mutant could not be activated even under viral infection. One possibility is that IRF3-2S sites have unknown function to mediate the activation of downstream 5ST sites rather than simply being phosphorylated. In our work, we demonstrated that S386 phosphorylation and pyrophosphorylation play a critical regulatory role for virus-induced phosphorylation of 5ST and transactivation activities of IRF3. UAP1-mediated pyrophosphorylation of S386 enhanced its binding affinity to TBK1, which is essential for the subsequent phosphorylation of IRF3 at 5ST sites to reach its full activity. When 5ST was substituted with the 5D, it will constitutively activate its DNA-binding ability, and there is no need for the phosphorylation and pyrophosphorylation of upstream serines including S386. Our data also showed that UAP1 no longer affected the activity of IRF3-5D. In addition, we observed that although IRF3 T390 was pyrophosphorylated, TBK1 failed to phosphorylate T390 on IRF3, and it is worth to identify the potential kinase for IRF3-T390 phosphorylation under viral infection in the future study.

Pyrophosphorylation was originally considered to be a non-enzymatic process,[31] and its function in immune signaling is unknown. Here, we identified UAP1 as a protein pyrophosphorylase, thereby positively regulating type I IFN signaling against viral

Figure 5. TNP inhibits type I IFN signaling as well as antiviral response

(A and B) Luciferase activity of HEK293T cells transfected with empty vector or HA-UAP1, subsequently pretreated with DMSO or N^2-(*m*-Trifluorobenzyl) (TNP) (10 μM), together with an ISRE (A) or IFN-β (B) luciferase reporter, followed by intracellular poly (I:C) (IC pIC) (10 μg/mL) treatment or SeV (MOI = 1) infection for 10 h.

(C) qRT-PCR analysis of *IFNB, ISG15*, and *UAP1* mRNA level in A549 cells transfected with empty vector or HA-UAP1, pretreated with DMSO or TNP (10 μM) for 2 h followed by SeV (MOI = 1) infection for 10 h.

(D) Lung and liver sections were analyzed by H&E staining from 8-week-old mice injected intraperitoneally with DMSO or TNP (20 mg/kg body weight [BW]) followed by given intravenously injection of PBS or VSV (1×10^8 pfu/g) for 24 h. Scale bars, 100 μm.

(E and F) VSV levels in lung and liver were analyzed by immunoblot analysis (E) and qRT-PCR (F) from 8-week-old mice injected intraperitoneally with DMSO or TNP (20 mg/kg BW), followed by given intravenously injection of PBS or VSV (1×10^8 pfu/g) for 24 h.

(G and H) qRT-PCR analysis of *Ifnb* and *Isg15* mRNA levels in lung (G) and liver (H) from 8-week-old mice injected intraperitoneally with DMSO or TNP (20 mg/kg BW), followed by given intravenously injection of VSV (1×10^8 pfu/g) for 24 h were analyzed.

(I) Survival of 8-week-old mice injected intraperitoneally with DMSO or TNP (20 mg/kg BW) followed by given intravenously injection of PBS or VSV (1×10^8 pfu/g) (n = 10 per group).

(J) ELISA results of IFN-β secretion in serum from mice pretreated with DMSO or TNP (20 mg/kg BW) followed by given intravenously injection of PBS or VSV (1×10^8 pfu/g) for 24 h.

Data in (A)–(C) are expressed as mean ± SEM of three independent experiments. Data in (G), (H), and (J) are expressed as mean ± SD of 3 mice per group. Data in (F) are expressed as mean ± SD of 4 mice per group.

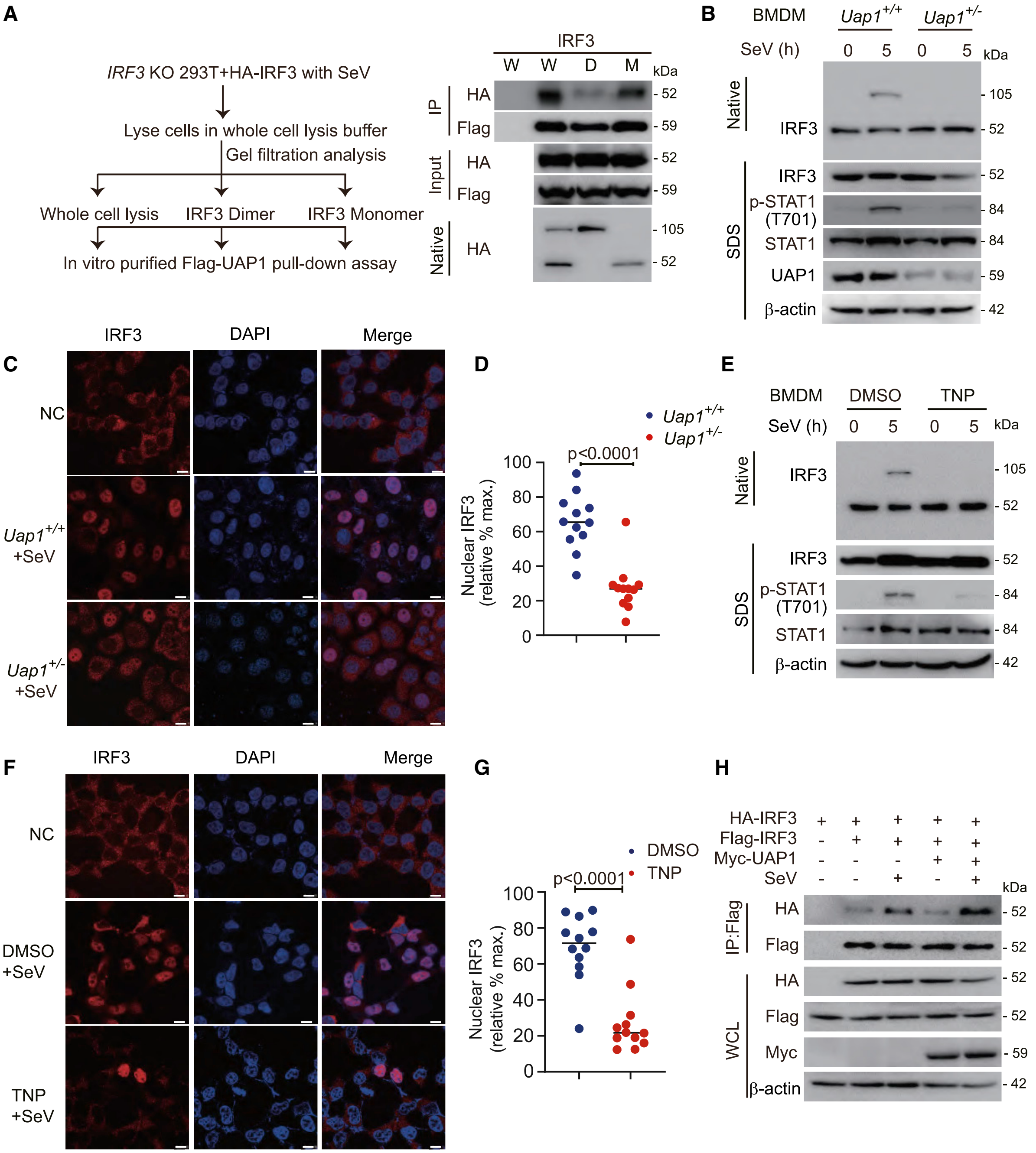

Figure 6. Pyrophosphorylation of IRF3 facilitates its activation

(A) Experimental setup for the isolation of IRF3 monomer and dimer from *IRF3* knockout (KO) HEK293T cells infected with SeV (MOI = 1) for 10 h (left). Immunoprecipitation and immunoblot analysis of *in-vitro*-purified Flag-UAP1 and whole-cell lysates (W), IRF3 monomer (M), or dimer (D) (right).

(B) Immunoblot analysis of IRF3 dimerization and STAT1 activation in BMDMs from $Uap1^{+/+}$ or $Uap1^{+/-}$ mice, infected with SeV for indicated time points.

(C) Immunofluorescence analysis of the nuclear translocation of IRF3 in BMDMs from $Uap1^{+/+}$ or $Uap1^{+/-}$ mice, infected with SeV for 5 h. Scale bars, 10 μm.

(D) The relative mean value of nuclear IRF3 in BMDMs from $Uap1^{+/+}$ or $Uap1^{+/-}$ mice, infected with SeV (MOI = 1, 5 h) were calculated by ImageJ.

(E) Immunoblot analysis of IRF3 dimerization and STAT1 activation in BMDMs pretreated with N^2-(*m*-Trifluorobenzyl) (TNP) (10 μM), infected with SeV for indicated time points.

(F) Immunofluorescence analysis of the nuclear translocation of IRF3 in BMDMs pretreated with TNP (10 μM) together with SeV (MOI = 1, 5 h). Scale bars, 10 μm.

(G) The relative mean value of nuclear IRF3 in BMDMs pretreated with TNP (10 μM) together with SeV (MOI = 1, 5 h) were calculated by ImageJ.

(H) Immunoblot analysis of HEK293T cells transfected with plasmids with indicated combinations, followed by IP with anti-Flag beads.

Data in (D) and (G) are expressed as mean ± SD of 12 cells per group. p values were determined by unpaired two-tailed Student's t test. All other experiments are representatives of three independent biological experiments with similar results.

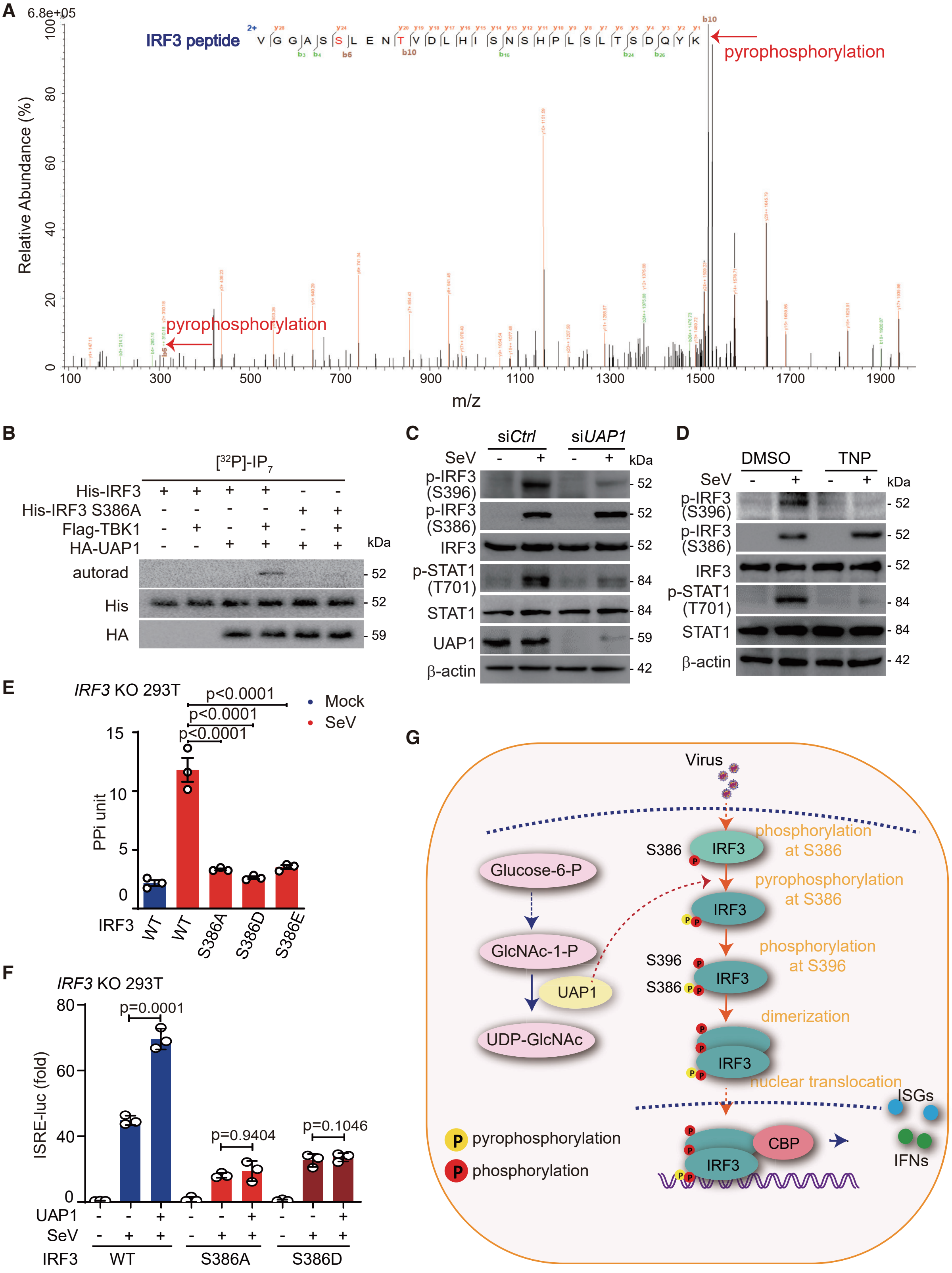

(legend on next page)

infection. Our findings illustrated the role of pyrophosphoserine residues in altering antiviral responses. Since the occurrence of protein pyrophosphorylation depends on phosphorylation, and this PTM has not attracted much attention in the past, the in-depth study of protein pyrophosphorylation may innovate the current understanding of the role of phosphorylation in cell signaling, and a large number of studies on the function of phosphorylation are worthy of re-evaluation.

In summary, we identified UAP1 as a positive regulator in type I IFN signaling by targeting IRF3 to promote its pyrophosphorylation. The working mechanism of UAP1 implies that metabolic enzymes are deeply involved in immune signaling pathways, thus keeping a precise control of the crosstalk between metabolism and innate antiviral immune responses.

Limitations of the study

This study uncovered the role of UAP1 as a pivotal regulator of antiviral innate immune responses by targeting IRF3 for pyrophosphorylation at S386. Although we demonstrated that UAP1 is responsible for IRF3 pyrophosphorylation by multiple methods including mass spectrometry analysis, autoradiography, PPi measurement assay, and *in vitro* phosphopeptide assay, it is necessary to develop specific antibodies against pyrophosphorylated proteins in future, which could greatly promote the research on the function of pyrophosphorylated proteins. We confirmed at UAP1 is not responsible for IRF3 pyrophosphorylation at T390, and the enzyme responsible for this modification is currently unknown. The physiological function of IRF3 pyrophosphorylation at T390 also needs to be further investigated. In addition, it is worth of study to figure out how UAP1 selectively recognizes pS386 and the exact binding site on TBK1 for pyrophosphorylated IRF3 in structural biology in future.

STAR★METHODS

Detailed methods are provided in the online version of this paper and include the following:

- KEY RESOURCES TABLE
- RESOURCE AVAILABILITY
  - ○ Lead contact
  - ○ Materials availability
  - ○ Data and code availability
- EXPERIMENTAL MODEL AND SUBJECT DETAILS
  - ○ Cell culture and transfections
  - ○ Antibodies and reagents
  - ○ Luciferase reporter assays
  - ○ Recombinant proteins
  - ○ Immunoprecipitation and immunoblot analysis
  - ○ Fluorescence resonance energy transfer (FRET)
  - ○ RNA extraction and quantitative RT-PCR
  - ○ Animals
  - ○ Histological assessment
  - ○ Generation of CRISPR/Cas9 knockout cell lines
  - ○ Small interfering RNA (siRNA) transfection
  - ○ Enzyme-linked immunosorbent assay (ELISA)
  - ○ Virus infection and titration
  - ○ Protein pyrophosphorylation assay
  - ○ Molecular docking
  - ○ Mass spectrometry analysis
  - ○ PPi measurement assay
  - ○ RNA sequencing analysis
- QUANTIFICATION AND STATISTICAL ANALYSIS

SUPPLEMENTAL INFORMATION

Supplemental information can be found online at https://doi.org/10.1016/j.molcel.2022.12.007.

ACKNOWLEDGMENTS

This work was supported by National Natural Science Foundation of China (32270922, 92042303, 31870862 and 8210061242) and Guangdong Basic and Applied Basic Research Foundation (2020B1515120090).

AUTHOR CONTRIBUTIONS

J.C. proposed the concept and conceived the entire study. S.Y., S.J., H.X., and Z.Z. performed most of the experiments, with assistance from L.W., Y.W., L.Z., and M.L. S.Y., S.J., and J.C. wrote the manuscript.

DECLARATION OF INTERESTS

The authors declare no competing interests.

Received: April 6, 2022
Revised: August 25, 2022
Accepted: December 9, 2022
Published: January 4, 2023

Figure 7. S386 in IRF3 is essential for UAP1-mediated pyrophosphorylation

(A) Flag-tagged IRF3 purified from *IRF3* knockout (KO) HEK293T cells transfected with Flag-IRF3, followed by SeV (MOI = 1) infection for 10 h were prepared for LC-MS/MS analysis. LC-MS/MS of the pyrophosphorylated peptide fragment ion was shown. Sequence of IRF3 with MS/MS coverage was listed. Red residues: pyrophosphorylation site.

(B) Pyrophosphorylation of wild-type (WT) IRF3 and IRF3 S386A mutant were measured by autoradiography *in vitro*. Flag-tagged TBK1 and HA-UAP1 were purified from HEK293T cells, and His-tagged WT IRF3 and IRF3 S386A mutant were purified from *E. coli*. All experiments are representatives of three independent biological experiments with similar results.

(C) Immunoblot analysis of extracts of A549 cells transfected with control siRNA or *Uap1*-specific siRNA, then infected with SeV (MOI = 1) for 5 h.

(D) Immunoassay of extracts of A549 cells pretreated with N^2-(*m*-Trifluorobenzyl) (TNP) (10 μM) and infected with SeV (MOI = 1) for 5 h.

(E) PPi was measured by fluorimetry assay in *IRF3* KO HEK293T cells transfected with plasmid of WT IRF3 and its indicated mutants (S386A, S386D, and S386E), infected with SeV (MOI = 1) for 5 h, followed by immunoprecipitation with anti-Flag beads.

(F) Luciferase activity of *IRF3* KO HEK293T cells transfected with vectors of IRF3 (WT, S386A or S386D), together with an ISRE luciferase reporter and UAP1, infected with SeV (MOI = 1) for 10 h.

(G) The working model of the precise regulation of IRF3 activity mediated by UAP1 through pyrophosphorylation.

Data in (E) and (F) are expressed as mean ± SEM of three independent experiments. p values were determined by unpaired two-tailed Student's t test. All other experiments are representatives of three independent biological experiments with similar results.

REFERENCES

1. Takeuchi, O., and Akira, S. (2010). Pattern recognition receptors and inflammation. Cell *140*, 805–820. https://doi.org/10.1016/j.cell.2010.01.022.
2. Medzhitov, R., and Janeway, C.A., Jr. (1997). Innate immunity: the virtues of a nonclonal system of recognition. Cell *91*, 295–298. https://doi.org/10.1016/s0092-8674(00)80412-2.
3. Gürtler, C., and Bowie, A.G. (2013). Innate immune detection of microbial nucleic acids. Trends Microbiol. *21*, 413–420. https://doi.org/10.1016/j.tim.2013.04.004.
4. Buck, M.D., Sowell, R.T., Kaech, S.M., and Pearce, E.L. (2017). Metabolic instruction of immunity. Cell *169*, 570–586. https://doi.org/10.1016/j.cell.2017.04.004.
5. Dai, Z.W., Ramesh, V., and Locasale, J.W. (2020). The evolving metabolic landscape of chromatin biology and epigenetics. Nat. Rev. Genet. *21*, 737–753. https://doi.org/10.1038/s41576-020-0270-8.
6. Diskin, C., Ryan, T.A.J., and O'Neill, L.A.J. (2021). Modification of proteins by metabolites in immunity. Immunity *54*, 19–31. https://doi.org/10.1016/j.immuni.2020.09.014.
7. Mukai, K., Konno, H., Akiba, T., Uemura, T., Waguri, S., Kobayashi, T., Barber, G.N., Arai, H., and Taguchi, T. (2016). Activation of STING requires palmitoylation at the Golgi. Nat. Commun. *7*, 11932. https://doi.org/10.1038/ncomms11932.
8. Li, T., Li, X., Attri, K.S., Liu, C., Li, L., Herring, L.E., Asara, J.M., Lei, Y.L., Singh, P.K., Gao, C., et al. (2018). O-GlcNAc transferase links glucose metabolism to MAVS-mediated antiviral innate immunity. Cell Host Microbe *24*, 791–803.e6. https://doi.org/10.1016/j.chom.2018.11.001.
9. Bhandari, R., Saiardi, A., Ahmadibeni, Y., Snowman, A.M., Resnick, A.C., Kristiansen, T.Z., Molina, H., Pandey, A., Werner, J.K., Juluri, K.R., et al. (2007). Protein pyrophosphorylation by inositol pyrophosphates is a posttranslational event. Proc. Natl. Acad. Sci. USA *104*, 15305–15310. https://doi.org/10.1073/pnas.0707338104.
10. Saiardi, A., Bhandari, R., Resnick, A.C., Snowman, A.M., and Snyder, S.H. (2004). Phosphorylation of proteins by inositol pyrophosphates. Science *306*, 2101–2105. https://doi.org/10.1126/science.1103344.
11. Saiardi, A. (2016). Protein pyrophosphorylation: moving forward. Biochem. J. *473*, 3765–3768. https://doi.org/10.1042/BCJ20160710C.
12. Azevedo, C., Burton, A., Ruiz-Mateos, E., Marsh, M., and Saiardi, A. (2009). Inositol pyrophosphate mediated pyrophosphorylation of AP3B1 regulates HIV-1 Gag release. Proc. Natl. Acad. Sci. USA *106*, 21161–21166. https://doi.org/10.1073/pnas.0909176106.
13. Chanduri, M., Rai, A., Malla, A.B., Wu, M., Fiedler, D., Mallik, R., and Bhandari, R. (2016). Inositol hexakisphosphate kinase 1 (IP6K1) activity is required for cytoplasmic dynein-driven transport. Biochem. J. *473*, 3031–3047. https://doi.org/10.1042/BCJ20160610.
14. Chen, X., Raimi, O.G., Ferenbach, A.T., and van Aalten, D.M.F. (2021). A missense mutation in a patient with developmental delay affects the activity and structure of the hexosamine biosynthetic pathway enzyme AGX1. FEBS Lett. *595*, 110–122. https://doi.org/10.1002/1873-3468.13968.
15. Chang, Y.H., Weng, C.L., and Lin, K.I. (2020). O-GlcNAcylation and its role in the immune system. J. Biomed. Sci. *27*, 57. https://doi.org/10.1186/s12929-020-00648-9.
16. Rusinova, I., Forster, S., Yu, S., Kannan, A., Masse, M., Cumming, H., Chapman, R., and Hertzog, P.J. (2013). Interferome v2.0: an updated database of annotated interferon-regulated genes. Nucleic Acids Res. *41*, D1040–D1046. https://doi.org/10.1093/nar/gks1215.
17. Duplaquet, L., Leroy, C., Vinchent, A., Paget, S., Lefebvre, J., Vanden Abeele, F., Lancel, S., Giffard, F., Paumelle, R., Bidaux, G., et al. (2020). Control of cell death/survival balance by the MET dependence receptor. eLife *9*, e50041. https://doi.org/10.7554/eLife.50041.
18. Peneff, C., Ferrari, P., Charrier, V., Taburet, Y., Monnier, C., Zamboni, V., Winter, J., Harnois, M., Fassy, F., and Bourne, Y. (2001). Crystal structures of two human pyrophosphorylase isoforms in complexes with UDPGlc(Gal)NAc: role of the alternatively spliced insert in the enzyme oligomeric assembly and active site architecture. EMBO J. *20*, 6191–6202. https://doi.org/10.1093/emboj/20.22.6191.
19. Boehmelt, G., Wakeham, A., Elia, A., Sasaki, T., Plyte, S., Potter, J., Yang, Y., Tsang, E., Ruland, J., Iscove, N.N., et al. (2000). Decreased UDP-GlcNAc levels abrogate proliferation control in EMeg32-deficient cells. EMBO J. *19*, 5092–5104. https://doi.org/10.1093/emboj/19.19.5092.
20. Asthana, A., Ramakrishnan, P., Vicioso, Y., Zhang, K., and Parameswaran, R. (2018). Hexosamine biosynthetic pathway inhibition leads to AML cell differentiation and cell death. Mol. Cancer Ther. *17*, 2226–2237. https://doi.org/10.1158/1535-7163.MCT-18-0426.
21. Allison, D.F., Wamsley, J.J., Kumar, M., Li, D., Gray, L.G., Hart, G.W., Jones, D.R., and Mayo, M.W. (2012). Modification of RelA by O-linked N-acetylglucosamine links glucose metabolism to NF-kappaB acetylation and transcription. Proc. Natl. Acad. Sci. USA *109*, 16888–16893. https://doi.org/10.1073/pnas.1208468109.
22. Pathak, S., Borodkin, V.S., Albarbarawi, O., Campbell, D.G., Ibrahim, A., and van Aalten, D.M. (2012). O-GlcNAcylation of TAB1 modulates TAK1-mediated cytokine release. EMBO J. *31*, 1394–1404. https://doi.org/10.1038/emboj.2012.8.
23. DeVito, S.R., Ortiz-Riaño, E., Martínez-Sobrido, L., and Munger, J. (2014). Cytomegalovirus-mediated activation of pyrimidine biosynthesis drives UDP-sugar synthesis to support viral protein glycosylation. Proc. Natl. Acad. Sci. USA *111*, 18019–18024. https://doi.org/10.1073/pnas.1415864111.
24. Werner, J.K., Jr., Speed, T., and Bhandari, R. (2010). Protein pyrophosphorylation by diphosphoinositol pentakisphosphate (InsP7). Methods Mol. Biol. *645*, 87–102. https://doi.org/10.1007/978-1-60327-175-2_6.
25. Ghoshal, S., Zhu, Q., Asteian, A., Lin, H., Xu, H., Ernst, G., Barrow, J.C., Xu, B., Cameron, M.D., Kamenecka, T.M., et al. (2016). TNP [N2-(m-trifluorobenzyl), N6-(p-nitrobenzyl)purine] ameliorates diet induced obesity and insulin resistance via inhibition of the IP6K1 pathway. Mol. Metab. *5*, 903–917. https://doi.org/10.1016/j.molmet.2016.08.008.
26. Lin, R., Mamane, Y., and Hiscott, J. (1999). Structural and functional analysis of interferon regulatory factor 3: localization of the transactivation and autoinhibitory domains. Mol. Cell. Biol. *19*, 2465–2474. https://doi.org/10.1128/MCB.19.4.2465.
27. Servant, M.J., Grandvaux, N., tenOever, B.R., Duguay, D., Lin, R., and Hiscott, J. (2003). Identification of the minimal phosphoacceptor site required for in vivo activation of interferon regulatory factor 3 in response to virus and double-stranded RNA. J. Biol. Chem. *278*, 9441–9447. https://doi.org/10.1074/jbc.M209851200.
28. Takahasi, K., Suzuki, N.N., Horiuchi, M., Mori, M., Suhara, W., Okabe, Y., Fukuhara, Y., Terasawa, H., Akira, S., Fujita, T., et al. (2003). X-ray crystal structure of IRF-3 and its functional implications. Nat. Struct. Biol. *10*, 922–927. https://doi.org/10.1038/nsb1001.
29. Suhara, W., Yoneyama, M., Iwamura, T., Yoshimura, S., Tamura, K., Namiki, H., Aimoto, S., and Fujita, T. (2000). Analyses of virus-induced homomeric and heteromeric protein associations between IRF-3 and coactivator CBP/p300. J. Biochem. *128*, 301–307. https://doi.org/10.1093/oxfordjournals.jbchem.a022753.
30. Qin, B.Y., Liu, C., Lam, S.S., Srinath, H., Delston, R., Correia, J.J., Derynck, R., and Lin, K. (2003). Crystal structure of IRF-3 reveals mechanism of autoinhibition and virus-induced phosphoactivation. Nat. Struct. Biol. *10*, 913–921. https://doi.org/10.1038/nsb1002.
31. Harmel, R., and Fiedler, D. (2018). Features and regulation of non-enzymatic post-translational modifications. Nat. Chem. Biol. *14*, 244–252. https://doi.org/10.1038/nchembio.2575.
32. Cui, J., Li, Y., Zhu, L., Liu, D., Songyang, Z., Wang, H.Y., and Wang, R.F. (2012). NLRP4 negatively regulates type I interferon signaling by targeting the kinase TBK1 for degradation via the ubiquitin ligase DTX4. Nat. Immunol. *13*, 387–395. https://doi.org/10.1038/ni.2239.

33. Qin, Y., Liu, Q., Tian, S., Xie, W., Cui, J., and Wang, R.F. (2016). TRIM9 short isoform preferentially promotes DNA and RNA virus-induced production of type I interferon by recruiting GSK3beta to TBK1. Cell Res. *26*, 613–628. https://doi.org/10.1038/cr.2016.27.

34. Jin, S., Tian, S., Chen, Y., Zhang, C., Xie, W., Xia, X., Cui, J., and Wang, R.F. (2016). USP19 modulates autophagy and antiviral immune responses by deubiquitinating Beclin-1. EMBO J. *35*, 866–880. https://doi.org/10.15252/embj.201593596.

35. Wu, Y., Zhou, T., Hu, J., Liu, Y., Jin, S., Wu, J., Guan, X., and Cui, J. (2022). Autophagy activation induces p62-dependent autophagic degradation of dengue virus capsid protein during infection. Front. Microbiol. *13*, 889693. https://doi.org/10.3389/fmicb.2022.889693.

36. Zheng, Y., Liu, Q., Wu, Y., Ma, L., Zhang, Z., Liu, T., Jin, S., She, Y., Li, Y.P., and Cui, J. (2018). Zika virus elicits inflammation to evade antiviral response by cleaving cGAS via NS1-caspase-1 axis. EMBO J. *37*, e99347. https://doi.org/10.15252/embj.201899347.

37. Trott, O., and Olson, A.J. (2010). AutoDock Vina: improving the speed and accuracy of docking with a new scoring function, efficient optimization, and multithreading. J. Comput. Chem. *31*, 455–461. https://doi.org/10.1002/jcc.21334.

38. Ma, J., Chen, T., Wu, S., Yang, C., Bai, M., Shu, K., Li, K., Zhang, G., Jin, Z., He, F., et al. (2019). iProX: an integrated proteome resource. Nucleic Acids Res. *47*, D1211–D1217. https://doi.org/10.1093/nar/gky869.

39. Chen, T., Ma, J., Liu, Y., Chen, Z., Xiao, N., Lu, Y., Fu, Y., Yang, C., Li, M., Wu, S., et al. (2022). iProX in 2021: connecting proteomics data sharing with big data. Nucleic Acids Res. *50*, D1522–D1527. https://doi.org/10.1093/nar/gkab1081.

40. Pertea, M., Kim, D., Pertea, G.M., Leek, J.T., and Salzberg, S.L. (2016). Transcript-level expression analysis of RNA-seq experiments with HISAT, StringTie and Ballgown. Nat. Protoc. *11*, 1650–1667. https://doi.org/10.1038/nprot.2016.095.

41. Huang, da W., Sherman, B.T., and Lempicki, R.A. (2009). Systematic and integrative analysis of large gene lists using DAVID bioinformatics resources. Nat. Protoc. *4*, 44–57. https://doi.org/10.1038/nprot.2008.211.

STAR★METHODS

KEY RESOURCES TABLE

REAGENT or RESOURCE	SOURCE	IDENTIFIER
Antibodies		
Rabbit polyclonal anti-IRF3	Santa Cruz Biotechnology	Cat# sc-9082; RRID: AB_2264929
Anti-STAT1	Santa Cruz Biotechnology	Cat# sc-136; RRID: AB_675899
Goat anti-mouse	Santa Cruz Biotechnology	Cat# sc-2005; RRID: AB_631736
Goat anti-rabbit	Santa Cruz Biotechnology	Cat# sc-2004; RRID: AB_631736
Rabbit monoclonal anti-IRF3 phosphorylated at S396	Cell Signaling Technology	Cat# sc-166583; RRID: AB_2012300
Rabbit monoclonal anti-TBK1 phosphorylated at S172	Cell Signaling Technology	Cat# sc-8017; RRID: AB_628423
Rabbit polyclonal anti-TBK1	Cell Signaling Technology	Cat# 3013; RRID: AB_2199749
Anti-mouse IgG (H+L), F(ab′)2 Fragment (Alexa Fluor® 488 Conjugate)	Cell Signaling Technology	Cat# 14119-1-AP; RRID: AB_2140168
Anti-rabbit IgG (H+L), F(ab′)2 Fragment (Alexa Fluor® 555 Conjugate)	Cell Signaling Technology	Cat# 4947; RRID: AB_823547
Rabbit monoclonal anti-phospho-IRF3 (Ser386)	Cell Signaling Technology	Cat# 37829; RRID: AB_2799121
Rabbit polyclonal anti-phospho-STAT1	Cell Signaling Technology	Cat# 9171; RRID: AB_331591
Rabbit monoclonal anti-OGT	Cell Signaling Technology	Cat# 5368; RRID: AB_303264
Rabbit monoclonal anti-UAP1	Proteintech	Cat# 67545-1-Ig, RRID: AB_2882762
Rabbit monoclonal anti-O-GlcNAc	Abcam	Cat# ab2739; RRID: AB_303264
Mouse monoclonal anti-Flag (M2) peroxidase (HRP)	Sigma-Aldrich	Cat# 5483P; RRID: AB_10693472
Mouse monoclonal anti-β-actin	Sigma-Aldrich	Cat# 3738; RRID: AB_490837
Hemagglutinin (HA)-HRP antibody	Roche Applied Science	Cat# 12994; RRID: AB_2630393
Mouse monoclonal anti-c-Myc-HRP	Roche Applied Science	Cat# 3013; RRID: AB_2199749
Rabbit polyclonal anti-IRF3	Santa Cruz Biotechnology	Cat# sc-9082; RRID: AB_2264929
Anti-STAT1	Santa Cruz Biotechnology	Cat# sc-136; RRID: AB_675899
Goat anti-mouse	Santa Cruz Biotechnology	Cat# sc-2005; RRID: AB_631736
Goat anti-rabbit	Santa Cruz Biotechnology	Cat# sc-2004; RRID: AB_631736
Bacterial and Virus Strains Chemicals		
Vesicular stomatitis virus-eGFP	Cui et al.[32]	N/A
Sendai virus	Qin et al.[33]	N/A
Human influenza virus A/Puerto Rico/8/34 (H1N1) (PR8)	Jin et al.[34]	N/A
Dengue virus (strain 16681)	Wu et al.[35]	N/A
ZIKV (GZ01, KU820,898)	Zheng et al.[36]	N/A
Biological samples		
Mouse tissue	C57BL/6J $Uap1^{+/+}$ and $Uap1^{+/-}$ mice	N/A
Human PBMCs	This paper; see cell culture and transfections in experimental model section	N/A
Chemicals, peptides, and recombinant proteins		
PBS	Coring	Cat# 21-040-CV
DMEM	Coring	Cat# 10-013-CVR
poly(I:C) (LMW)	Invivogen	Cat# tlrl-picw
poly(dA:dT)	Invivogen	Cat# tlrl-patn

(Continued on next page)

Continued

REAGENT or RESOURCE	SOURCE	IDENTIFIER
Polybrene	Sigma-Aldrich	Cat# H9268
Puromycin	Sigma-Aldrich	Cat# P9620
Flag-beads	Sigma-Aldrich	Cat# A2220
NP-40	Solarbio	Cat# N8030
Protein A agarose	Pierce	Cat# 20333
Protein G agarose	Pierce	Cat# 20399
Phosphatase inhibitor	Roche Applied Science	Cat# 04906837001
HA-beads	Roche Applied Science	Cat# 12013819001
EDTA-free protease inhibitor	Biosharp	Cat# BL630B
Paraformaldehyde	Meilunbio	Cat# MA0192
Fetal bovine serum	Gibco	Cat# 1099-141
L-glutamine	Gibco	Cat# 25030-081
RPMI 1640 medium	Gibco	Cat# C22400500BT
Macrophage colony-stimulating factor (MCSF)	PeproTech	Cat# AF-315-02
Granulocyte colony-stimulating factor (GCSF)	PeproTech	Cat# AF-300-03
Lipofectamine 2000	Invitrogen	Cat# 11668019
Lipofectamine RNAiMAX	Invitrogen	Cat# 13778100
jetPRIME	Polyplus Transfection	Cat# 114-01
Adenosine triphosphate (ATP)	InvivoGen	Cat# tlrl-atpl
$\gamma[^{32}P]$ ATP	Perkin Elmer,	Cat# NEG002A
Tris	GCRF, China	Cat# RS000135
NaCl	GCRF, China	Cat# RS9971
$MgCl_2$	Vetec	Cat# V900020
EDTA	Vetec	Cat# V900106
Glycerol	Vetec	Cat# V900122
Critical commercial assays		
HiScript III RT SuperMix for qPCR (+gDNA wiper)	Vazyme	Cat# R323-01
2×PolarSignal SYBR Green mix Taq (with Tli RNaseH)	MIKX	Cat# MKG900-10
EZ-press RNA Purification Kit	EZBioscience	Cat# B0004D
Human IFN-β ELISA kit	Invivo gene	Cat# luex-hifnbv2
Mouse IFN-β ELISA kit	Invivo gene	Cat# luex-mifnbv2
Dual-Glo® Luciferase Assay System	Promega	Cat#E2980
CytoTox 96 Non-Radioactive Cytotoxicity kit	Promega	Cat# G1780
Deposited data		
Original western data for figures	This paper	https://data.mendeley.com/datasets/5w7rt5mxxp/2
Mass Spectrometry	This paper	PXD: PXD038295
RNA-seq raw data	This paper	SAR: PRJNA868602
Experimental models: Cell lines		
HEK293T	ATCC	CRL-11268
IRF3 KO HEK293T	This paper	N/A
HeLa	ATCC	CCL-2
A549	ATCC	CRM-CCL-185
Experimental models: Organisms/strains		
C57BL/6J	Guangzhou Medical Laboratory Animal Center of China	GDMLAC-O7
C57BL/6J *Uap1*$^{+/-}$ mice	This paper	N/A

(*Continued on next page*)

Continued

REAGENT or RESOURCE	SOURCE	IDENTIFIER
Oligonucleotides		
siRNA targeting sequence: *Ctrl* UUCUCCGAACGUGUCACGUTT	This paper	N/A
siRNA targeting sequence: *UAP1* #1: 5′-AGACGUCUUGGACAACUGATT-3′	This paper	N/A
siRNA targeting sequence: *UAP1* #2: 5′-AGUAGCAGUUCUUCUUCUATT-3′	This paper	N/A
sgRNA targeting sequence: *UAP1*: 5′-TCGGCGTTGCATATCCTAAG-3′	This paper	N/A
sgRNA targeting sequence: *IRF3*: 5′-CTTGTACTGGTCGGAGGTGA-3′	This paper	N/A
sgRNA targeting sequence: *HK II*: 5′-CCGTGTTCGGAATGGGAAGT-3′	This paper	N/A
sgRNA targeting sequence: *G6PD*: 5′-CTTGTACTGGTCGGAGGTGA-3′	This paper	N/A
sgRNA targeting sequence: *GFPT*: 5′-GTTGCTCGGCAGGTAAGTCG-3′	This paper	N/A
sgRNA targeting sequence: *PKM*: 5′-TTGGACGGTGCAACCGAGCT-3′	This paper	N/A
sgRNA targeting sequence: *PFK*: 5′-CCTACAACCTGGTGAAGCGT-3′	This paper	N/A
sgRNA targeting sequence: *LDHA*: 5′-CCCGATTCCGTTACCTAATG-3′	This paper	N/A
sgRNA targeting sequence: *CS*: 5′-CAGCCGAACCAAGTACTGGG-3′	This paper	N/A
sgRNA targeting sequence: *ODGH*: 5′-GACTAGTTCGAACTATGTGG-3′	This paper	N/A
sgRNA targeting sequence: *IDH*: 5′-AACGTTGCACACTAACGGGA-3′	This paper	N/A
sgRNA targeting sequence: *IP6K1*: 5′-TGAGACGCATCTCAGACCGG-3′	This paper	N/A
Primers for qRT-PCR, see Table S1	This paper	N/A
Recombinant DNA		
Plasmid: pcDNA3.1-Flag/HA/Myc for all transient expression vectors	This paper	N/A
Flag-tagged IRF3 and constructs	This paper	N/A
HA-tagged UAP1 and constructs	This paper	N/A
Flag-tagged UAP1	This paper	N/A
Myc-tagged UAP1	This paper	N/A
pET28a containing IRF3	This paper	N/A
pET28a containing IP6K1	This paper	N/A
pECFP-C1 containing UAP1	This paper	N/A
pEYFP-C1 containing IRF3	This paper	N/A
leti-CRISPR v2 vector	Addgene	Plasmid # 52961
Software and algorithms		
Image Lab	Bio-Rad Laboratories, inc.	http://www.bio-rad.com/zhcn/product/image-lab-software
Leica LAS AF	Leica Microsystem	N/A
GraphPad Prism 8	GraphPad software, inc.	http://www.graphpad.com
ImageJ	National Institutes of Health	https://imagej.nih.gov/ij
PyMol	Schrödinger, Inc.	https://pymol.org/2/

(*Continued on next page*)

Continued

REAGENT or RESOURCE	SOURCE	IDENTIFIER
SPCImage 3.10	Becker & Hickl	N/A
ImageJ	National Institutes of Health	https://imagej.nih.gov/ij
data.table R package v. 1.14.0	R Core Team	https://rdatatable.gitlab.io/data.table/
stringdist R package v. 0.9.6.3	R Core Team	https://github.com/markvanderloo/stringdist
FlowJo	Tree Star software, inc.	https://www.flowjo.com
ggplot2 R package v. 3.3.3	R Core Team	https://cran.r-project.org/ web/packages/ggplot2/index.html
Autodock Vina	The Center for Computational Structural Biology	https://Vina.scripps.edu

RESOURCE AVAILABILITY

Lead contact

Further information and requests for reagents may be directed to and will be fulfilled by the lead contact Jun Cui (cuij5@mail.sysu.edu.cn).

Materials availability

This study did not generate new unique reagents and plasmids and cell lines are listed in the key resources table and available for use upon request to the lead contact.

Data and code availability

- Original western blots imaging data generated in this study are publicly available on Mendeley data: https://data.mendeley.com/datasets/5w7rt5mxxp/2. The DOI is listed in the key resources table. RNA-seq data generated during this study are deposited at the SRA under access number: PRJNA868602. Mass spectrometry data is deposited at proteomeXchange database via the iProX partner repository and made available at the following accession number: PXD038295. The dataset identifier for these data is list in the key resources table.
- This study does not report original code.
- Any additional information required to reanalyze the data reported in this paper is available from the lead contact upon request.

EXPERIMENTAL MODEL AND SUBJECT DETAILS

Cell culture and transfections

HEK293T (human embryonic kidney HEK293T) cells and A549 cells obtained from the Cell Bank of the Chinese Academy of Sciences (Shanghai, China) were cultured in Dulbecco's modified Eagle's medium (DMEM) (CORNING, 10-013-CVR), supplemented with 10% fetal bovine serum (Gibco) and 1% L-glutamine (Gibco). Bone marrow cells (BMs) were isolated from randomly chosen 8-week-old of wild-type or *Uap1*$^{+/-}$ mice and then BMs were differentiated into bone marrow-derived macrophages (BMDMs) cultured in 10 ml conditioned medium (DMEM medium with 10 % fetal bovine serum, 1 % L-glutamine, penicillin-streptomycin (Gibco,1:100), 100 ng/ml macrophage colony-stimulating factor (PeproTech). BMs were differentiated into bone marrow-derived dendritic cells (BMDCs) cultured with RPMI 1640 containing 10% fetal bovine serum, 1% L-glutamine, penicillin-streptomycin, and 100 ng/ml granulocyte-macrophage colony stimulating factor (PeproTech). On day 3, most cells were adherent to the dish. Discard the medium from the dish, and then the dish was supplemented with 10 ml of conditioned medium for further growth until day 6. On day 7, the cells were used to perform the experiments. Peripheral blood mononuclear cells (PBMCs) were isolated from blood from healthy donors (Zhongshan School of Medicine) collected in BD Vacutainer CPT tubes. PBMCs were cultured with RPMI 1640 containing 10% fetal bovine serum, 1% L-glutamine, and penicillin-streptomycin. The using of PBMCs was duly in compliance with institutional guidelines and approved protocols by Sun Yat-sen University, and all healthy donors signed a consent form approved by the Research Ethics Committee of the Sun Yat-sen University Cancer Center (GZR2013-040). All cells were incubated in 37 °C incubator with 5% CO_2. HEK293T cells were transfected for 30 h with a combination of overexpression plasmids with Lipofectamine 2000 reagent (Invitrogen, 11668019). BMDMs were transfected with Flag-UAP1 for 30 h with jetPRIME (Polyplus transfection, 114-01). Where indicated, cells were transfected with poly(I:C) (10 μg/ml) (InvivoGen) and poly(dA:dT) (5 μg/ml) (InvivoGen).

Antibodies and reagents

The following antibodies were used: Flag (M2) (1:5,000; Sigma-Aldrich, A8592), β-actin (1:5,000; Sigma-Aldrich, A1978), Myc-horseradish peroxidase (1:3,000; Roche, 11814150001), HA-peroxidase (high affinity from rat immunoglobulin G1) (1:3,000; Roche, 12013819001), His (1:2,000; Proteintech, HRP-66005), phospho-TBK1 (Ser172) (1:1,000; Cell Signaling Technology, 5483S), TBK1 (1:1,000; Cell Signaling Technology, 3013), phospho-IRF3 (Ser396) (1:1,000; Cell Signaling Technology, 4947S), phospho-IRF3 (Ser386) (1:1,000; Cell Signaling Technology, 37829), phospho-STAT1 (Tyr386) (1:1,000; Cell Signaling Technology, 9171), OGT (1:1,000; Cell Signaling Technology, 5368), UAP1 rabbit mAb (1:2,000; Proteintech, 67545), Mouse-derived anti-O-Linked N-Acetylglucosamine (RL2) (1:1,000; Abcam, ab2739), IRF3 (1:1,000; Santa Cruz Biotechnology, sc-9082) and STAT1 (1:2,000; Santa Cruz Biotechnology, sc-136). OSMI-1 compound was purchased from Sigma Aldrich (SML1621). N_2-(m-Trifluorobenzyl) (TNP) was purchased from Sigma-Aldrich (519178280).

Luciferase reporter assays

Cells were seeded in 24-well plates and transfected with plasmids encoding the ISRE/IFN-β luciferase reporter (firefly luciferase, 100 ng) and TK luciferase reporter (Renilla luciferase, 10 ng) together with different plasmids. Cells were collected using passive lysis buffer and luciferase activity was measured with the Dual-Luciferase Assay (Promega, E1941), according to the manufacturer's protocol.

Recombinant proteins

All 6×His-tagged proteins (IRF3 WT, IRF3 S386A) were expressed and purified from *E. coli* strain BL21 (Thermo Scientific, EC0114). Cells were resuspended in His-lysis buffer (50 mM Tris-HCl pH 7.9, 150 mM NaCl, 1% Triton X-100, 2 mM DTT [Sigma, 10,197,777,001], 20 mM imidazole [Sigma, 56,750], and protease inhibitors [Roche, 11,697,498,001]) and lysed by sonication. After centrifugation and filtration, the extract was loaded onto Ni-NTA Columns (Thermo, R90110). After washing with lysis buffer for 5 times, the protein was eluted using lysis buffer containing 400 mM imidazole. The eluted proteins were dialyzed into TBS buffer (50 mM Tris-HCl pH 7.9, 150 mM NaCl, 5% glycerol and 3 mM beta-mercaptoethanol [Sigma, M3148]). For purification of proteins from HEK293T cells, Flag-TBK1, Flag-UAP1 and Flag-IRF3 were expressed by transient transfection and cells were harvested in low-salt lysis buffer. The lysates were incubated Anti-Flag M2 Affinity Gel (Sigma, A2220) after clearing the lysate by centrifugation. The bound material was eluted using lysis buffer containing 0.5 mg/mL 3 × Flag Peptide (APEX Bio, A6001) or 0.5 mg/ml Myc peptide (APEX Bio, A6003).

Immunoprecipitation and immunoblot analysis

Relevant cells were lysed in low-salt lysis buffer (50 mM HEPES, pH 8.0, 150 mM NaCl, 1 mM EDTA (Vetec), 1.5 mM $MgCl_2$, 10% glycerol, 1% Triton X-100 (Sigma-Aldrich, T9284), a phosphatase inhibitor cocktail (5 mg/mL; Roche, 04906837001) and EDTA-free protease inhibitor) and incubated on a rocker with ice for 30 min. Whole-cell lysates were centrifuged at 12,000 g/ 4 °C for 30 min and boiled at 100 °C for 5 min in 5×SDS loading buffer (FD Biotechnology, PD006). For immunoprecipitation experiments, whole-cell extracts were incubated with anti-Flag M2 affinity gel (Sigma-Aldrich, A2220) or Protein A agarose (Pierce, 20333) and protein G agarose (Pierce, 20399) overnight. The beads were washed 5 times with low-salt lysis buffer. The immunoprecipitates were boiled at 100 °C for 5 min in 2×SDS loading buffer. The proteins were resolved by SDS-PAGE and transferred into PVDF membrane (Bio-Rad) and incubated with the appropriate antibodies. The membranes were further incubated with the indicated antibodies and detected with Immobilon Western Chemiluminescent HRP Substrate (Millipore). Images were performed using the ChemiDoc MP System (Bio-Rad) and Image Lab version 6.0 (Bio-Rad software, California, USA).

Fluorescence resonance energy transfer (FRET)

A549 cells were seeded into 35 mm glass-bottom dishes (Nest Scientific, 801002) and transfected with indicated plasmids. Two days post-transfection, cells were fixed with 4% paraformaldehyde washed and mounted in PBS. FRET assay was performed on a Leica TCS SP8 confocal microscopy system, using FRET SE (sensitized emission) Leica software modules. At 460-nm excitation, FRET was calculated as the ratio of YFP to CFP intensity. FRET efficiency was calculated as follows: EFRET = 1 T_{DA}/T_D, from measurement of the donor intensity values in presence of the acceptor (T_{DA}) and the donor alone intensity values (T_D) in reference. GraphPad Prism 8 is used to plot the FRET results.

RNA extraction and quantitative RT-PCR

Total RNA was extracted by Trizol reagent (Invitrogen, 15596018) according to the manufacturer's instructions. Reverse-transcribed into cDNA using HiScript III RT SuperMix for qPCR (+gDNA wiper) (Vazyme). Quantitative RT-PCR was performed with the 2× PolarSignal SYBR Green mix Taq (with Tli RNaseH) (MIKX). Data shown are the relative abundance of the indicated mRNA derived from human or mouse normalized by the standard of GAPDH. Gene-specific primer sequences were listed in Table S1.

Animals

C57BL/6J *Uap1*$^{+/-}$ mice were generated by CRISPR/Cas9 technology. C57BL/6J WT mice (GDMLAC-O7) were purchased from Guangzhou Medical Laboratory Animal Center of China. Animals were kept and bred in specific pathogen-free barrier facilities with standard conditions of temperature (20-25 °C) and humidity (30-70 %) 12-h light–dark cycles (lights on at 8:00 a.m. and off 8:00 p.m.) at Sun Yat-sen University. Institutional Animal Care and Use Committee of Sun Yat-sen University approved all the experimental protocols concerning the handing of mice. 8-week-old mice were used in the experiments. All animal experiments were performed according to the institutional guidelines at Sun Yat-Sen University (SYXK (YUE) 2017-0175, Guangzhou, China).

Histological assessment

The mice were euthanized by CO_2 from compressed gas cylinders. The tissues were fixed in 4 % paraformaldehyde for more than 24 h, and embedded in paraffin. The sections (thickness, 6 μm) were stained with hematoxylin & eosin Y (Servicebio, China). Hematoxylin & eosin-stained sections were analyzed by microscope (DMi8; Leica).

Generation of CRISPR/Cas9 knockout cell lines

We analyzed single-guide RNA (sgRNA) in the website http://crispr.mit.edu/ and chose the sequences with the highest score to design primers, sequences were listed in key resources table. Annealing products were annealed and then linked to the pCRISPR-V2 vector.

The sgRNA sequences of *IRF3* were as follows:
Forward 5'-CACCGTTGGAAGCACGGCCTACGGC -3’
Reverse 5'-AAACGCCGTAGGCCGTGCTTCCAAC-3’
The sgRNA sequences of *UAP1* were as follows:
Forward 5'-CACCGTCGGCGTTGCATATCCTAAG-3',
Reverse 5'-AAACCTTAGGATATGCAACGCCGAC-3';

The Cas9 lentiviral plasmid used in our lab (Addgene plasmid no. 108100) harbors a puromycin-resistance marker, and Cas9-expressing cells were selected using 1μg/ml puromycin (Thermo Fisher Scientific, A1113803). After HEK293T cells were seeded, medium was replaced with DMEM containing lentiviruses expressing Cas9 and specific sgRNAs, and polybrene (10 μg/ml) (Sigma-Aldrich) was added for 48 h. Cells were then selected by puromycin (Sigma-Aldrich) for 5 days, and polyclonal pools of cells were generated for clonal screening and following experiments. Then the single clone was picked up for expansion with another round of puromycin selection for 2 weeks. The knockout efficiency was checked by sequencing and immunoblot analysis.

Small interfering RNA (siRNA) transfection

Chemically synthesized siRNA duplexes were obtained from Transheep (Shanghai, China) and transfected using Lipofectamine RNAiMAX (Invitrogen) according to the manufacturer’s instructions. RNA oligonucleotides used are as follows:

Control siRNA, 5′-UUCUCCGAACGUGUGUCACGUTT-3′
UAP1 siRNA #1, 5′-AGACGUCUUGGACAACUGATT-3′
UAP1 siRNA #2, 5′-AGUAGCAGUUCUUCUUCUATT-3′

Enzyme-linked immunosorbent assay (ELISA)

Cells were stimulated with viruses or transfected with plasmids. The supernatants were collected for measurement of IFN-β by ELISA kit. 8-week-old $Uap1^{+/+}$ and $Uap1^{+/-}$ mice were intravenously injected with VSV (1×10^8 pfu/g) or HSV-1 (2×10^7 pfu/g) for 24 h, and then the serum samples were absorbed from coagulated blood for measurement of IFN-β by ELISA kit according to the manufacturer’s protocols. ELISA kits for human IFN-β (luex-hifn-β) and mouse IFN-β (luex-mifn-β) were purchased from InvivoGen.

Virus infection and titration

Cells were infected with SeV (MOI=1), VSV (MOI=1), HSV-1 (MOI=1), H1N1 (MOI=5), DENV-2 (strain 16681) (MOI=1) or ZIKV (GZ01, KU820,898) (MOI=1) for indicated time periods. For *in vivo* studies, age- and sex-matched mice were infected by intravenous injection with HSV-1 (2×10^7 pfu/g) or VSV (1×10^8 pfu/g). For virus infection survival experiments, mice were monitored for survival after viral infection. Virus titers were determined from the 50% of the tissue culture’s infectious dose (TCID50). Cells were infected at different multiplicity of infections (MOI).

Protein pyrophosphorylation assay

$5\beta[^{32}P]$ IP_7 was produced by phosphorylation of IP_6 using IP6K1 and $\gamma[^{32}P]$ ATP (Perkin Elmer, NEG002A).[10] Recombinant IRF3 was incubated with affinity-purified TBK1 from HEK293T cells in kinase buffer [25 mM Tris-HCl (pH 7.5), 5 mM β-glycerophosphate, 2 mM DTT, 0.1 mM Na_3VO_4, 10 mM $MgCl_2$]. After 30 min of incubation, the reaction was stopped and purified for p-IRF3. For *in vitro* pyrophosphorylation, protein extracts were incubated in IP_7 phosphorylation buffer [25 mM Hepes (pH 7.4), 50 mM NaCl, 6 mM MgCl2, 1 mM DTT] and 1 μCi $5\beta[^{32}P]$ IP_7 for 15 min at 37°C. The reactions were heated at 95°C for 5 min in sample buffer before separation by NuPAGE (Invitrogen, Carlsbad, CA). Radiolabeled proteins were detected by SDS-PAGE (The gel strips were subsequently dried and subjected to autoradiography).

Molecular docking

Molecular docking was performed using docking program on Autodock Vina.[37] Autodock Vina requires the input files of the receptor macromolecule (UAP1, 1JVG) and ligands (IP_7) in a PDBQT format along with the configuration file which contain parameters (gridbox size: size x=74.55, size y=74.55, size z=74.55 and gridbox center points in terms of x=-29.673, y=9.314, z=24.341, energy range=4, exhaustiveness=12, num-modes=10). Perl scripts were used to prepare these configuration files and run the Vina program.

Mass spectrometry analysis

Total lysates were prepared from *IRF3* KO HEK293T cells transfected with Flag-IRF3 and followed by immunoprecipitation with α-Flag M2 beads. Immunoprecipitated proteins were separated by SDS-PAGE, and then stained with Coomassie Blue. The entire lane was excised, digested with trypsin, and analyzed with LC-MS/MS. LC-MS/MS identification of peptide mixtures was performed once with two replicates per condition at BIOPROFILE TECHNOLOGY (Shanghai, China). Briefly, peptides were chromatographed through Easy-nLC1200 (Thermo Fisher, California, USA). Peptide samples were loaded by Trap column (reverse-phase), (100 μm* 2 cm, 5μm, C18, Dr. Maisch GmbH) and separated by Thermo scientific EASY column (75 μm*15 cm, 3 μm, C18) at 300 nL min^{-1} for 60 min using a four-step acetonitrile (0.1% formic acid in 80% acetonitrile) gradient: 25% over the first 2 min and 5–28% for 2–44 min and 28–40% for 44–51 min and 40–100% for 51–53 min. The tandem mass spectrometry was performed by Q Exactive mass spectrometer (Thermo Fisher, California, USA). The MS1 survey scan (350–1800 m/z) was at a resolution of 60,000 at 200 m/z with automatic gain control (AGC) target of 3e6 and a maximum injection time of 50 ms. Dynamic exclusion was 60.0 s. Each full scan takes 20 MS2 scans. MS2 activation type was HCD model. Isolation window was 2 m/z. The MS2 survey was at a resolution of 15,000 at 200 m/z with automatic gain control (AGC) target of 1e5 and a maximum injection time of 50 ms. RAW files generated by spectrometer was subjected to Proteome Discoverer (version 1.4) software with searching the library of Uniprot homo sapiens (uniprot-Homo sapiens (Human) [9606]-204995-20220606.fasta) for protein identification. Trypsin was specified as the proteolytic enzyme, with up to two missed cleavage sites allowed. Carbamidomethylation was set as the fixed modification. Oxidation (M) and ubiquitination [GlyGly (K)] were set as the variable modifications. The precursor mass tolerance was set to 20 ppm and the fragment ion tolerance at 0.1 Da. Proteins were identified based on at least one unique peptide. Protein and peptide identification confidence threshold were set to an FDR of 1%. The tandem mass spectra of matched peptides were checked manually for their validity. The mass spectrometry proteomics data have been deposited to the ProteomeXchange Consortium (http://proteomecentral.proteomexchange.org) via the iProX partner repository with the dataset identifier PXD038295.[38,39]

PPi measurement assay

All proteins (WT IRF3 or its indicated mutants) were produced in HEK293T cells, and purified with Flag beads and eluted with HEPES buffer. A last wash was performed in phosphate buffer without sorbitol, and cells were pelleted and resuspended in 500 μl of HEPES buffer (pH 7). The protein concentration was determined using a Pierce BCA Protein Assay kit (Thermo Scientific, 23227). The Flag-tagged phosphopeptides were synthesized by ChinaPeptides Co., LTD. All these peptides were characterized by HPLC-MS/MS and purity (not lower than 95%) was determined by HPLC-UV (220 nm). In brief, 1 mg of each peptide was dissolved in 200 μL of solvent (100% H_2O). 5 mg/mL of each peptide mentioned above was used for pyrosphosphate (PPi) measurement assay. For pyrosphosphate (PPi) measurement assay, equivalent protein quantities of cell lysate preparation were added to a 96-well flat-bottom black plate (Greiner Bio-one). PPi was measured using a PhosphoWorks fluorimetric pyrophosphate assay kit (AAT Bioquest, 21614) following the manufacturer's protocol. The kit provided a chemical tool, PPi sensor, which could be used to visualize this modification on protein. The PPi sensor used in the kit has quite high selectivity to PPi compared to phosphate and ATP. Additionally, this reagent showed minimal interactions with other anionic functional groups. Briefly, 50 μl of various samples were incubated with 50 μl of PPi Sensor working solution, incubated the reaction at room temperature for 10–30 minutes, monitored the fluorescence increase with a fluorescence plate reader at Ex/Em = 370/470 nm.

RNA sequencing analysis

Total RNA of BMDMs was extracted by TRIzol (Invitrogen, 10296010), high-throughput sequencing was carried out based Illumina MiSeq platform in Shanghai Sangon Biotech Co., Ltd. following the manufacturer's recommendations. Quality control of the raw fastq data was done with FastQC. All clean data were mapped to the mouse reference genome (mm10) using histat2.[40] The aligned SAM file was converted into sorted BAM files by SAMtools, and the HTSeq-count program was used to count the total number of reads that are mapped to the genome. To identify differentially expressed genes (DEGs) of all samples, DESeq2 v.1.28.1 was used to normalize reads counts. P value < 0.05 and fold-change ≥ 2 were determined as DEGs using Bioconductor clusterProfiler package v3.14.3 for the functional enrichment of DEGs. The DAVID tool was used for GO analysis by applying default parameters, except that only those transcripts fulfilling the condition of FPKM > 0.2 in the input samples were set as background.[41] The column plots were generated based on the enriched GO terms using the ggplot2 in R package. All genes were annotated to Kyoto Encyclopedia of Genes and Genomes (KEGG) pathways using KAAS (KEGG Automatic Annotation Server). RNA-seq sequence density profiles were normalized per 10 million reads using bedtools in R package and visualized in IGV genome browser. The *UAP1* differential gene expression profiles were also subjected to gene set enrichment analysis (GSEA). GSEA was performed using GSEA software.

QUANTIFICATION AND STATISTICAL ANALYSIS

The data of all quantitative *in vitro* experiments are represented as mean ± SEM of three independent experiments; data are reported as means ± SD of 3–10 mice per group. Images were analyzed with ImageJ. Statistical analyses were done using the software Graphpad Prism version 8.0 (GraphPad Software, Inc, La Jolla, CA, USA). MantelCox test and Gehan–BreslowWilcoxon test were used for mice survival analysis. Unpaired two-tailed Student's *t* test with a *P*-value < 0.05 considered statistically significant between groups was used for all statistical analyses.